EFDA–JET–R(13)04

I.T. Chapman, M. Becoulet, T. Bird, J. Canik, M. Cianciosa, W. Cooper,
T. Evans, N. Ferraro, C. Fuchs, J. Graves, M. Gryaznevich, Y. Gribov, C. Ham,
J. Hanson, G. Huysmans, S. Jardin, A. Kirk, L. Lao, S. Lazerson, Y. Liang,
I. Lupelli, R. Moyer, C. Neuhrenberg, F. Orain, D. Orlov, S. Sabbagh,
W. Suttrop , Y. Suzuki, K. Tritz, E. Unterberg, D. Yadykin,
the ASDEX Upgrade, DIII-D, MAST and NSTX Teams
and EFDA-JET contributors

# 3d Distortion of the Plasma Boundary in the Presence of Saturated MHD Instabilities or Applied Resonant Magnetic Perturbations
# ITPA MHD Working Group 12
# Final Report

# 3d Distortion of the Plasma Boundary in the Presence of Saturated MHD Instabilities or Applied Resonant Magnetic Perturbations ITPA MHD Working Group 12 Final Report

I.T. Chapman[1], M. Becoulet[2], T. Bird[3], J. Canik[4], M. Cianciosa[5], W. Cooper[6], T. Evans[7], N. Ferraro[7], C. Fuchs[8], J. Graves[6], M. Gryaznevich[9], Y. Gribov[10], C. Ham[1], J. Hanson[5], G. Huysmans[10], S. Jardin[11], A. Kirk[1], L. Lao[7], S. Lazerson[11], Y. Liang[12], I. Lupelli[1], R. Moyer[7], C. Neuhrenberg[3], F. Orain[2], D. Orlov[13], S. Sabbagh[14], W. Suttrop[8], Y. Suzuki[15], K. Tritz[16], E. Unterberg[4], D. Yadykin[17], the ASDEX Upgrade, DIII-D, MAST and NSTX Teams and EFDA-JET contributors*

*[1]EURATOM/UKAEA Fusion Association, Culham Science Centre, OX14 3DB, UK.*
*[2]CEA, IRFM, F-13108 Saint-Paul-lez-Durance, France*
*[3]Max-Planck-Institut fur Plasmaphysik, 17491 Greifswald, Germany*
*[4]Oak Ridge National Laboratory, Oak Ridge, Tennessee 37831-8071, USA*
*[5]Auburn University, Physics Department, Auburn, AL 36849, USA*
*[6]CRPP, Association EURATOM/Conf´ed´eration Suisse, EPFL, 1015 Lausanne, Switzerland*
*[7]General Atomics, PO Box 85608, San Diego, CA 92186, USA*
*[8]Max-Planck-Institut fur Plasmaphysik, EURATOM-Ass D-85748 Garching, Germany*
*[9]Tokamak Solutions, Culham Science Centre, Oxon, UK*
*[10]ITER Organisation, Route de Vinon sur Verdon, St-Paul-lez-Durance, France*
*[11]PPPL, Princeton University, PO Box 451, Princeton, NJ 08543, USA*
*[12]Forschungszentrum Ju¨lich GmbH, IEF-4, 52425 J¨Ulich, Germany*
*[13]University of California, San Diego, USA*
*[14]Department of Applied Physics and Applied Mathematics, Columbia University, New York, USA*
*[15]National Institute for Fusion Science, Toki, Japan*
*[16]Johns Hopkins University, Baltimore, MD, USA*
*[17]EURATOM/VR Association, Chalmers University, Gothenburg, Sweden*
**See the Appendix of F. Romanelli et al., Fusion Energy 2012*
*(Proc. 24th Int. Conf. San Diego, 2012) IAEA, (2012)*

**Abstract.**

The three dimensional plasma boundary displacements induced by either long-lasting core MHD instabilities or by applied non-axisymmetric magnetic perturbations have been measured in ASDEX Upgrade, DIII-D, JET, MAST and NSTX. For the core instabilities, the displacements are usually small, although in extreme cases in MAST when the rotation braking is strong and global a significant displacement can be observed. The most concerning instability for ITER is the saturated internal kink, or helical core, which can be found in plasmas with a wide region of low magnetic shear such as the hybrid scenario, which can lead to non-negligible boundary displacements. Nonetheless, the boundary displacement resultant from core MHD instabilities in ITER is predicted to be less than $\pm 1\%$ of the minor radius.

The displacements arising from applied resonant magnetic perturbations (RMPs) are measured up to $\pm 5\%$ of the minor radius in present day machines. Good agreement has been found between these experimental measurements and a range of models – from vacuum field line tracing, to ideal three dimensional MHD equilibrium reconstruction, to nonlinear plasma amplification. The measured displacement across a range of machines is found to correlate linearly with the applied resonant field predicted by vacuum modelling. The RMP-induced displacements foreseen in ITER are expected to lie within the range of those predicted by the different models, meaning less than $\pm 1.75\%$ ($\pm 3.5$cm) of the minor radius in the H-mode baseline and less than $\pm 2.5\%$ ($\pm 5$cm) in a 9MA plasma. Whilst a displacement of 7cm peak-to-peak in the baseline scenario is marginally acceptable from both a plasma control and heat loading perspective, it is important that ITER adopts a plasma control system which can account for a three dimensional boundary corrugation to avoid an $n = 0$ correction which would otherwise exacerbate the displacement caused by the applied fields.

## 1. Introduction and Background

Previous results [1, 2, 3, 4, 5, 6, 7] have shown that either the presence of core instabilities or the application of resonant magnetic perturbations can cause significant non-axisymmetric distortions to the plasma boundary. Such perturbations to the boundary could lead to unacceptable heat loads on the plasma facing components in ITER. The allowable plasma displacement to avoid damage to the first wall has been assessed as 8cm with three-dimensional scrape-off layer transport modelling [8], whilst the boundary must stay within a 4cm envelope of its set-point to achieve good RF coupling [9]. Consequently it is important that we can predict the likely distortions in ITER and prepare methods for the avoidance or control of such boundary displacements.

Past experiments to measure the plasma perturbation when non-axisymmetric perturbation fields are applied have been performed on DIII-D [1, 7], ASDEX Upgrade [2, 3, 4], MAST [5, 6] and JET [5]. In some DIII-D discharges the plasma response to $n = 1$ fields was found to amplify the edge perturbation [1], whilst in both MAST and JET L-mode plasmas and other DIII-D cases with $n = 3$ RMPs [7], the displacement of the edge of the plasma showed no signs of plasma amplification and scaled approximately linearly with the applied field. Nonetheless, in all cases, applied fields from either ex- or in-vessel field correction coils had a demonstrable and significant effect on the toroidal periodicity of the plasma edge, deforming the separatrix by a few percent of the minor radius.

Measurements of the displacements caused by core MHD are described in section 2 and compared to numerical modelling in section 3. Measurements of the displacements caused by applied non-axisymmetric magnetic perturbations are presented in section 4 and compared to numerical modelling in section 5. Finally, predictions for the displacements expected in ITER due to core MHD or externally applied RMPs are made in sections 6 and 7 respectively.

## 2. Measurements of displacements due to core MHD in present machines

There are various conditions under which fusion plasmas are susceptible to long-lasting plasma instabilities which can give rise to displacements of the plasma boundary. For the purposes of this study, we discount any displacements arising due to transient events since these distortions are especially hard to model numerically and therefore extrapolation of likely distortions in ITER is problematic. It has been observed in many devices that in plasmas with a wide region of low magnetic shear and $q \geq 1$, the plasma exhibits long-lasting $n = 1$ ideal MHD instabilities [10, 11, 12, 13, 14]. Similarly, neoclassical tearing modes can exist for multiple energy confinement times [11, 15, 16, 17] and resistive wall modes controlled by magnetic feedback can also be sustained for a long time [18, 24, 20, 22]. Routinely, the boundary displacement due to such instabilities is of secondary concern, even though it does lead to a noticeable level of non-axisymmetry and can cause large displacements under certain conditions.

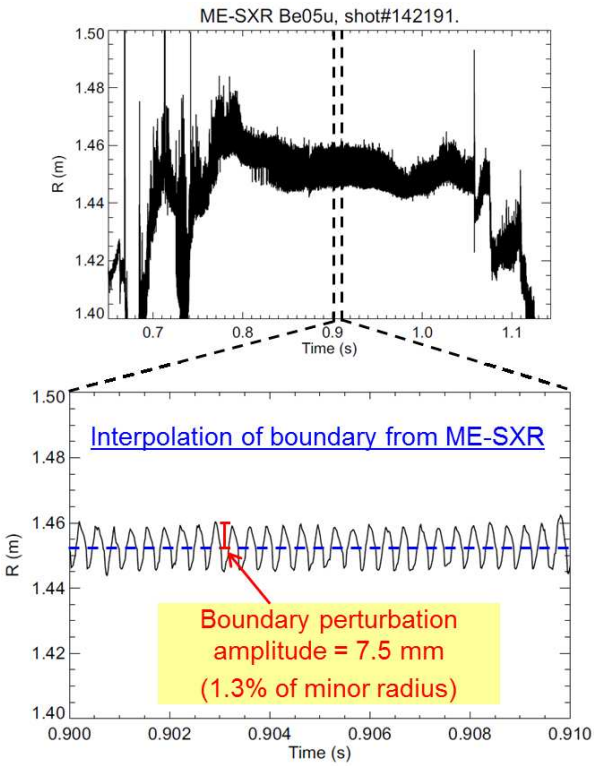


**Figure 1.** The plasma boundary measured by the Multi-Energy Soft X-ray system in NSTX for a discharge with a core saturated 1/1 kink mode coupled to a 2/1 tearing mode, showing a displacement of 1.3% of the minor radius.

Hereafter we are only concerned by edge displacements due to saturated MHD instabilities. Edge displacements have been measured with the multi-energy soft X-ray system on NSTX in the presence of both core-localised MHD instabilities and also for an external kink. The multi-energy soft X-ray cameras have 1cm radial resolution between channels near the plasma edge, and interpolation allows sub-cm resolution. An $n = m = 1$ internal kink mode in plasmas with low-shear above $q = 1$ has been found to couple to $m/n = 2/1$ tearing modes, giving rise to islands of 10cm, equating to 15% of the minor radius [23]. The position of the boundary in the presence of a 1/1 kink coupled to a 2/1 tearing mode, which can persist for half the length of the plasma discharge in NSTX, is illustrated in figure 1. It is evident that the plasma boundary is distorted by $\pm 7.5$mm, or $\pm 1.3\%$ of the minor radius.

Even larger displacements are measured in the case of less core-localised MHD instabilities. High normalised pressure plasmas often exhibit saturated global $n = 1$ kink instabilities, or resistive wall modes, which can persist for long times in the presence of magnetic feedback [24]. Whilst this low frequency mode activity is global and perturbs the plasma core, it also gives rise to significant shifts of the plasma boundary. Figure 2 shows the plasma boundary, again diagnosed by the SXR camera, showing a displacement of $\pm 0.95$cm, or $\pm 1.6\%$ of the minor radius, when there is a saturated $n = 1$ kink mode in a high $\beta_N$ NSTX plasma.

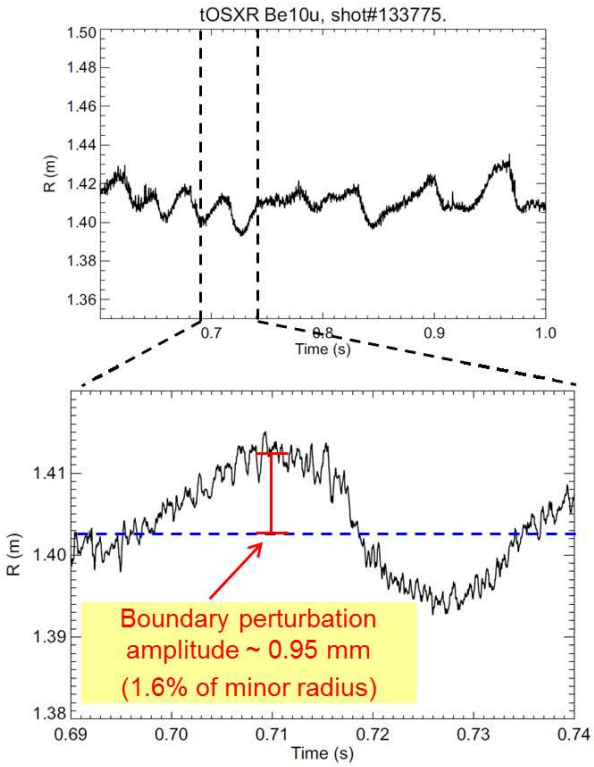


**Figure 2.** The plasma boundary measured by the Multi-Energy Soft X-ray system in NSTX for a discharge with an n=1 external kink/RWM, showing a displacement of 1.6% of the minor radius.

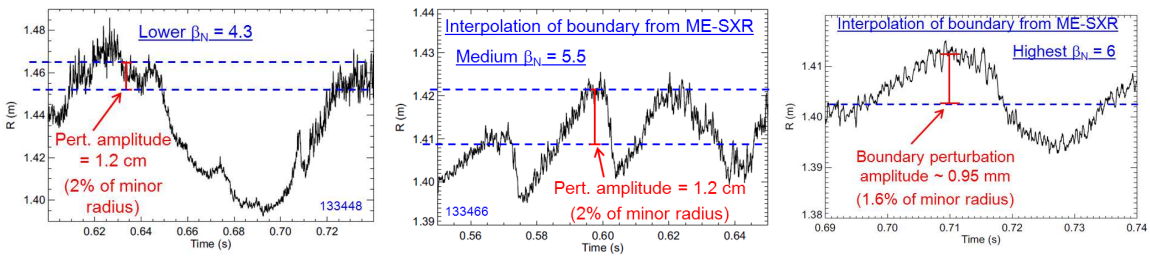


**Figure 3.** The plasma boundary measured by the Multi-Energy Soft X-ray system in NSTX for a discharge with an n=1 external kink/RWM at (left) $\beta_N$ less than the no-wall limit, (middle) intermediate normalised pressure and (right) for high $\beta_N$ above than the no-wall limit

Finally, there is no correlation between the boundary displacement in the presence of such global $n = 1$ instabilities and the normalised pressure with respect to the no-wall limit. Figure 3 shows that the edge displacement is largely independent of $\beta_N$. This is not unexpected since it has been shown that the RWM stability depends sensitively on rotation and $l_i$ as well as normalised pressure, and often plasmas at intermediate levels of rotation (ie neither the fastest nor slowest rotating cases in NSTX) have the least stable modes as the kinetic damping is minimised [24, 21].

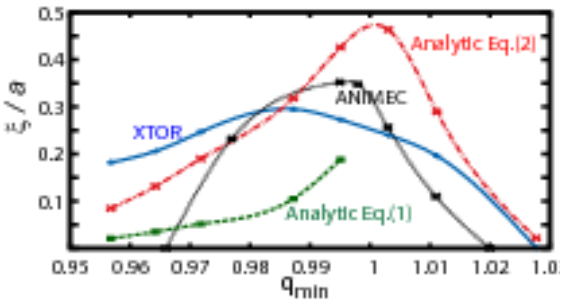


**Figure 4.** The displacement of the axis as a fraction of the minor radius as a function of the minimum safety factor as predicted by nonlinear MHD code, XTOR, showing good agreement with 3d equilibria produced by ANIMEC.

**** MAST DATA AND FIGURES HERE ****

## 3. Modelling of displacements due to core MHD in present machines

Saturated core instabilities such as those shown in section 2 can be modelled using three dimensional equilibrium codes, where the naturally-occurring helical core solution of a 3D equilibrium code is essentially the same as that from a non-linear MHD code (departing from an initially axisymmetric equilibrium) [25]. The Animec code [29] (an anisotropic version of the ideal 3d equilibrium code, Vmec [30]) has been used to simulate the boundary displacements expected in MAST when a helically displaced core is found in the equilibrium solution. Providing a reversed shear $q$-profile is used, and providing $q_{min}$ is sufficiently close to unity, two equilibria are found: One axisymmetric equilibrium, and the other a helical equilibrium with dominant $m = n = 1$ structure [26, 27, 28, 25]. The 3D, helical equilibrium can have slightly lower energy than its axisymmetric neighbour, and so it is in this sense, a preferred state. One can consider the saturated state of a non-linear MHD code equivalent to a 3D equilibrium [25]. This is exemplified by figure 4 which shows good agreement of the amplitude of the core displacement due to an $n = 1$ kink mode as found by a nonlinear MHD code, XTOR, compared to that found in a 3d equilibrium analysis using ANIMEC.

The midplane boundary position predicted by Animec is shown as a function of toroidal angle for a MAST plasma which exhibits a long-lived core kink mode [10] in figure 5. It is evident that the edge displacement caused by the core non-axisymmetry is negligible, and indeed smaller than the corrugation due to toroidal field ripple, which itself is much smaller than the perturbation due to applied resonant magnetic perturbations [6].

The boundary corrugation predicted in figure 5 is produced when only a small bootstrap current is included in the simulation. If the bootstrap current in the pedestal

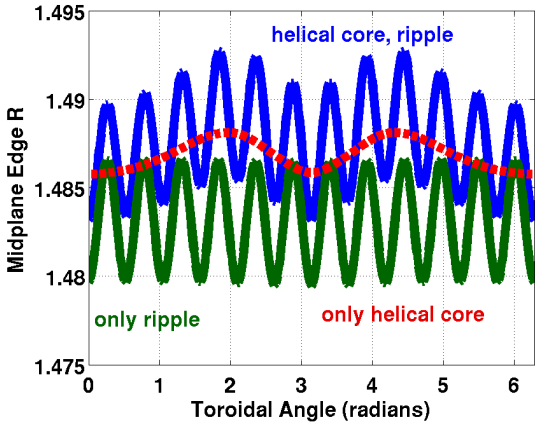


**Figure 5.** The midplane boundary position as a function of toroidal angle as modelled with ANIMEC for a MAST plasma with toroidal field ripple (green), a helical core (red), or both ripple and a helical core (blue).

region is (somewhat arbitrarily) increased, the boundary corrugation can become very significant. Figure 6 shows the boundary displacement in the presence of a large bootstrap current in the pedestal region. It is clear that the inclusion of a large bootstrap current results in a sizable boundary displacement, in this case up to 15cm compared to the case with low bootstrap current where the displacement was sub-cm. Figure 6 does not represent a realistic boundary corrugation, but exemplifies how the plasma distortion increases with the bootstrap current, which can be understood as an amplification of a current-driven mode near the plasma edge with the same helicity as the helical core.

Figure 6 also exemplifies the relative insensitivity of the boundary displacement to the amplitude of the helical core, as parameterised by the value of $q_{min}$ which dictates the susceptibility of the equilibrium to a non-axisymmetric branch. This is seen clearly in figure 7, where the boundary corrugation is of similar amplitude despite the helical core amplitude varying. The equilibrium is most susceptible to an internal kink for $q_{min}$ just above unity [31], and for $q_0 = 0.96, 1.05$ the saturated kink mode amplitude is smaller, yet the boundary displacement is relatively unchanged, again pointing to the important role played by the edge bootstrap current in causing this displacement.

Similar saturated core instabilities can be analysed using nonlinear MHD codes. The saturated state of the $n = m = 1$ ideal kink mode is tantamount to the helical core found in 3d equilibrium reconstruction. Such nonlinear MHD simulation has been performed using the M3D-C$^1$ code [32] for an NSTX plasma which exhibits a saturated core kink instability [33] (such as that which gives rise to the boundary displacement shown in figure 1). Figure 8 shows the electron temperature profiles before the onset of the kink mode compared to a time when the mode has a saturated amplitude. It is clear that whilst the core of the plasma is cooled and experiences a kink deformation, the boundary is negligibly affected.

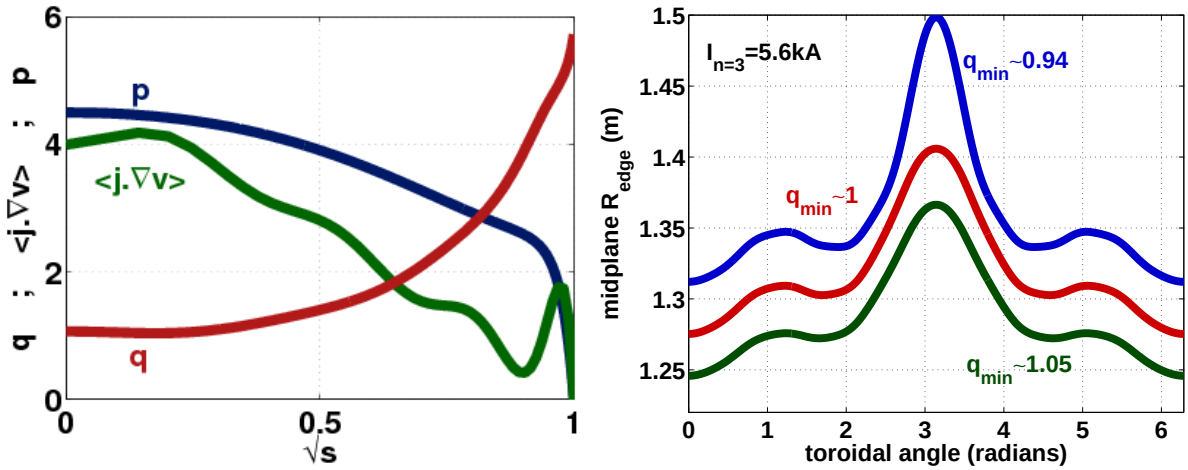


**Figure 6.** (left) The pressure, current density and $q$ profiles for a MAST plasma with inflated bootstrap current and (right) The midplane boundary position as a function of toroidal angle as modelled with ANIMEC for a MAST plasma with a helical core for different values of $q_{min}$ with a strong pressure pedestal included. An $n = 3$ RMP is included in the simulation to show how the $n = 1$ helical core displacement can dominate over the applied non-axisymmetric perturbation when the large bootstrap is included in the equilibrium.

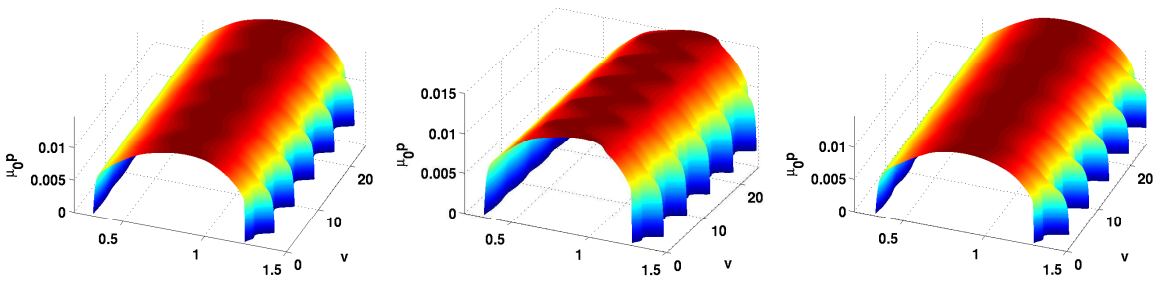


**Figure 7.** The plasma pressure as a function of radius and toroidal angle as modelled by ANIMEC for MAST plasmas with (left) $q_0 = 1.05$, (centre) $q_0 = 1.00$ and (right) $q_0 = 0.96$. In all cases there is a helical core, although its amplitude is maximised for $q_0 = 1.0$ and a corresponding boundary displacement.

## 4. Measurements of displacements due to RMPs in present machines

The effect of applying perturbations with different toroidal mode number has been investigated in MAST double null diverted (DND) plasmas optimised for diagnostic coverage. The primary diagnostics used to measure the radial position of the edge of the plasma are: the linear $D_\alpha$ camera which sees the edge of the plasma with a tangency plane in sector 12; the phantom colour camera which is tangent to sector 1; the charge exchange recombination spectroscopy diagnostic which views the neutral beam in sector 6; the RGB camera which views a tangency plane in sector 7; a charge-

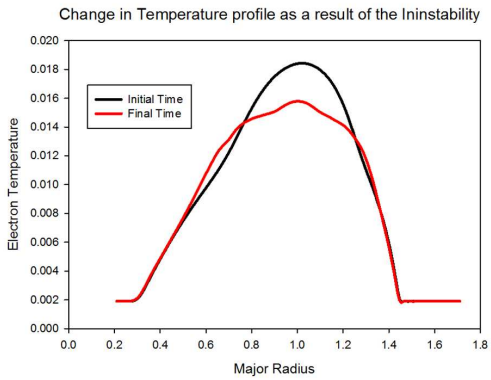


**Figure 8.** The electron temperature profiles in M3D-C[1] simulations of an NSTX plasma exhibiting a core kink instability, showing a large core displacement, but negligible change in the boundary position.

coupled device (CCD) camera viewing with a tangency plane approximately in sector 9; and the Thomson scattering diagnostic which has a lens in sector nine viewing the laser beam in sector eleven. Since there are twelve lower in-vessel coils in MAST, the phase of the $n = 3$ applied field can easily be changed in 30° quanta. In order to maximise the measurable perturbation of the edge of the plasma, two phases of an $n = 3$ RMP were applied with 60° between them. This has the added benefit that the position controller does not significantly correct for the distortion due to the applied RMPs as it is constrained by measurements of the plasma position in a sector experiencing a null in displacement for both phases of applied field. The radial position of the plasma boundary for six different high resolution diagnostics when the two phases of RMPs are applied (compared to a reference plasma in the absence of non-axisymmetric applied fields) is shown in figure 9 [6]. The expected toroidal phase dependence (with arbitrary amplitude) is added to guide the eye. It is clear that not only is there a different dependence of the edge corrugation in the two phases of the applied field, the toroidal variation follows the expected $n = 3$ periodicity symptomatic of the RMP applied. Furthermore, the amplitude of the displacement is found to be in good agreement on a number of different diagnostics and is approximately ±1.5cm, which represents more than ±2.5% of the minor radius [6].

A similar dependence is found when two phases of an $n = 4$ RMP field are applied, with figure 10 showing a clear $n = 4$ toroidal periodicity, again with an amplitude of toroidal corrugation of approximately ±1.5cm. In both figures 9 and 10 the position of the outboard midplane when RMPs are not applied is found to be in good agreement adding credence to the toroidal corrugation observed with RMPs.

Measurement of edge displacements have also been made in JET when $n = 2$ RMPs are applied from the set of ex-vessel error field correction coils (EFCCs) [36]. The direct measurements of the plasma boundary displacement are obtained using high resolution Thomson scattering (HRTS) diagnostic by following the time evolution

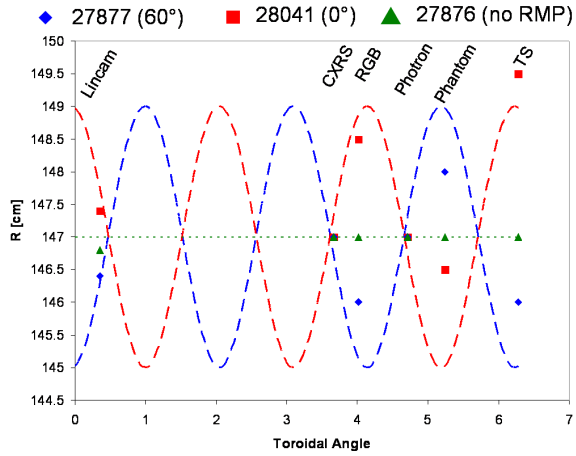


**Figure 9.** The midplane boundary position as a function of toroidal angle as measured by six different diagnostics with sub-cm radial resolution in MAST plasmas with two phases of an applied $n = 3$ RMP applied.

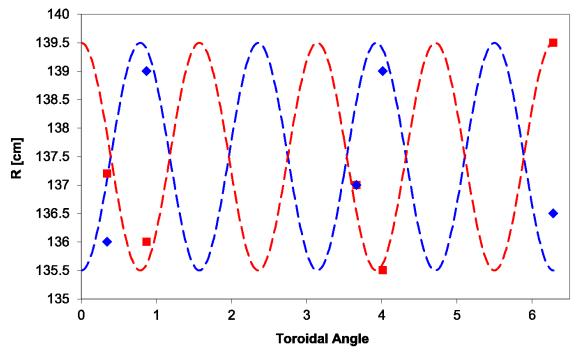


**Figure 10.** The midplane boundary position as a function of toroidal angle as measured by six different diagnostics with sub-cm radial resolution in MAST plasmas with two phases of an applied $n = 4$ RMP applied.

of the edge density profile as shown on figure 11 for the pulse 78151 with applied $I_{EFCC} = 1.75$ kA (much less than the upgraded maximum applicable coil current of 6kA). The procedure to determine the pedestal position takes into consideration the HRTS instrument function as described in reference [37]. The time evolution of the EFCC current, plasma boundary displacement measured by the HRTS (scaled to have zero displacement before application of the EFCC produced magnetic field) and the radial magnetic flux measured by the coincident flux loop for the shots with different values of the EFCC current are shown in figure 11. The effect of the field produced by EFCC coils on the plasma boundary is clearly seen in the kinetic measurements. Note a rapid change of the EFCC current signal is seen at $t = 58$s, attributed to the sudden loss of control of the EFCC power supply and, whilst not important for the present study, it clearly shows the dependence of the edge displacement on the applied field strength.

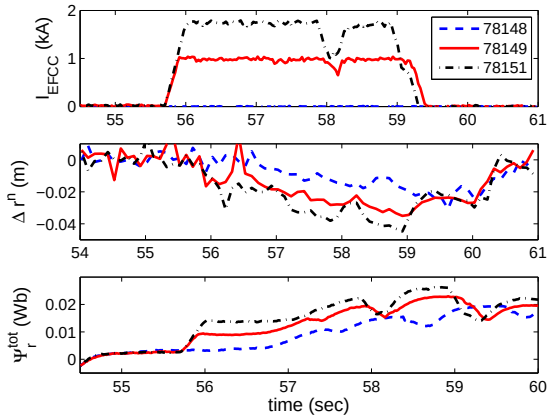


**Figure 11.** The RMP-induced displacement measured by the Thomson scattering diagnostic as a function of time (centre) compared to the coil in the ex-vessel coils in JET (top) and change in the magnetic flux (bottom).

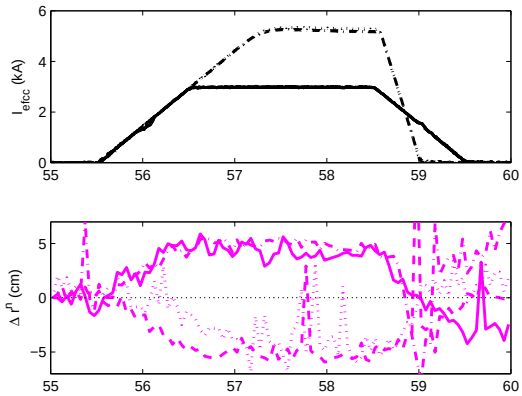


**Figure 12.** The RMP-induced displacement measured by the Thomson scattering diagnostic as a function of time compared to the coil in the ex-vessel coils in JET. The plasma position control is either done on the gap between the plasma boundary and the inner wall (dashed) or the outer wall (solid).

The response of the plasma controller, whilst not studied in detail, is striking. Figure 12 shows the measured displacement in JET when the plasma position feedback is either using the gap between the last closed flux surface and the magnetic loops on the centre column, or the outer gap between the plasma and the low-field side loops. It is evident that the plasma control system induces a shift in the opposite direction depending upon the position feedback scheme employed, with a very large discrepancy between these two schemes of 10cm. This exemplifies the acute need to account for non-axisymmetric displacements in the plasma position control feedback system.

In order to use magnetic measurements for the plasma boundary displacement studies, a calibration has been performed between the measured magnetic field and

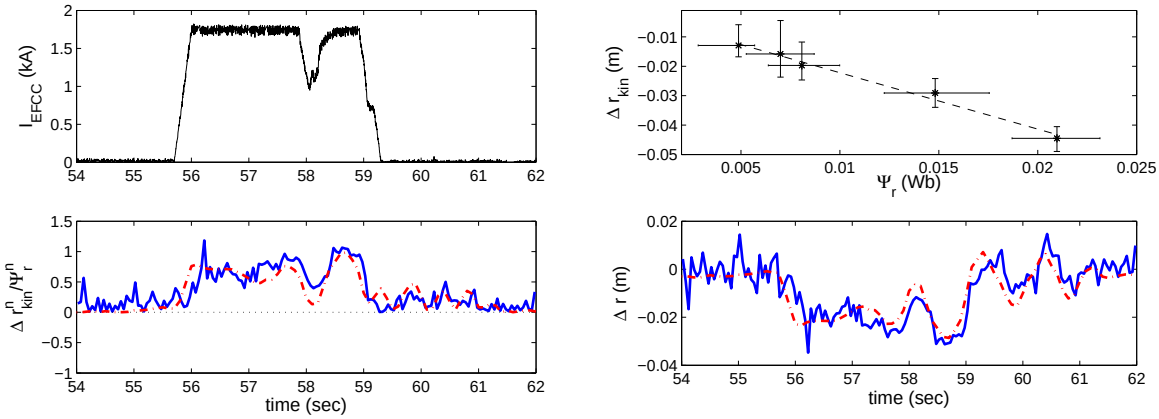


**Figure 13.** (left) The current in the ex-vessel coils in JET compared to the displacement measured by the Thomson scattering diagnostic (blue) and the calibrated magnetic signal on the midplane (red); (right) The linear scaling observed between the displacement given by Thomson scattering measurements compared to the change in the magnetic flux.

the displacement amplitude. As the majority of the saddle loops (excluding those in the divertor region) are within a few centimetres from the edge of the plasma, a linear extrapolation has been used in these studies, as shown in figure 13.

The response of the plasma boundary and separatrix to a 10Hz $n = 2$ rotating RMP has been studied on DIII-D using active imaging of the Doppler-shifted Balmer $D_\alpha$ emission from high energy injected neutrals (beam emission spectroscopy, BES) [43]. The measurements were obtained in ELMing H-mode discharges with lower single null (LSN) divertor and ITER-similar shape. The pedestal collisionality was selected to be similar to pedestal conditions predicted for ITER, $\nu_{,e} \sim 0.3$. Once a steady-state ELMing H-mode was established, the internal RMP coils were used to generate an $n = 2$ even parity RMP rotating counter to the plasma current in the toroidal direction at 10 Hz. This RMP field did not suppress the ELMs, but did result in significant periods of ELM mitigation, with the ELM frequency increasing and ELM amplitude decreasing. The temporal evolution of the measured beam emission at an elevation of $Z = 0.1$m is plotted in figure 14 as a function of major radius $R$. A coherent oscillation is clearly seen in the radius of the steep gradient region of the profile near $R = 2.30$m. In figure 14, the variation in the beam emission at $(R, Z) = (2.27, 0.1)$ is plotted versus time along with the RMP coil current. The beam emission intensity (thick, dashed red line) oscillates coherently and phase locked with the rotating $n = 2$ RMP (thin solid black line), with an amplitude of $\pm 1.5$cm, meaning $\pm 2.5\%$ of the minor radius [43].

In figure 15, the variation in the electron density profile at an elevation of $Z = 0.05$m on the LFS midplane as measured by profile reflectometry is plotted from 3-3.5ms in the same discharge used for the BES analysis described above. There is a clear coherent oscillation in the major radius $R$ of the steep edge gradient region of the profile as the

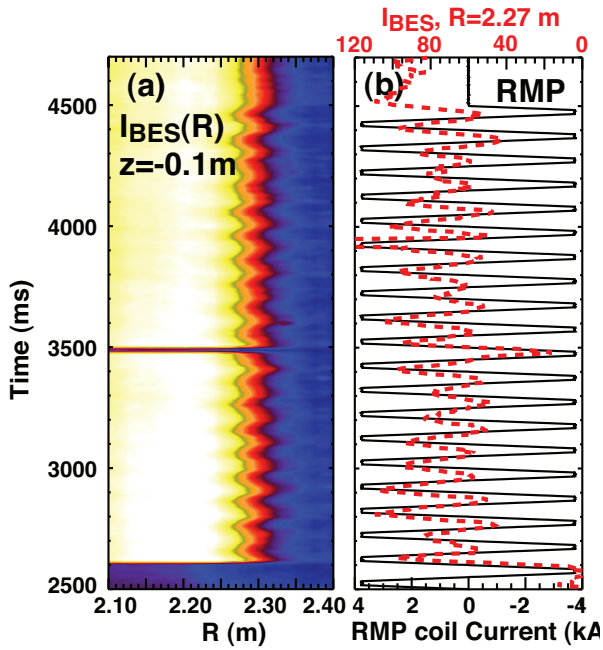


**Figure 14.** (a) Colour contours of the beam emission versus major radius R at an elevation of $z = 0.1$m on the outer midplane of the DIII-D tokamak during the RMP pulse. The rotating $n = 2$ field starts at 2250 ms (before the start of the plot), showing a coherent oscillation in phase with the rotating RMP. (b) Evolution of the rotating $n = 2$ RMP coil current in the upper 150° segment (thin black line), and the measured beam emission intensity (thick red dashed line) at $R = 2.27$m and $z = 0.1$m. The beam emission in the edge is modulated by the rotating $n = 2$ RMP.

$n = 2$ perturbation is rotated toroidally past the diagnostic which is qualitatively similar to the displacement measured in the beam emission intensity profile (figure 14). This displacement in the major radius of the steep edge gradient region is on the order of $\pm$1cm.

Finally, ASDEX Upgrade have also made measurements of the edge displacements when RMPs are applied [2, 4, 3]. A series of identical discharges with 1MA plasma current, a toroidal magnetic field of -2.4 T, fractional Greenwald density of $n_e/n_{GW} \sim$ 0.64, 9.7MW additional heating and 1kA saddle coil current has been performed, where only the configuration of the saddle coils has been varied: 2 discharges with mode number $n = 2$, odd up/down-parity (i.e. opposite polarity of upper and lower coils at the same toroidal position), with zero and 90 degrees toroidal orientation of the magnetic perturbations, and one discharge with n=2, even parity. The density profile measured by the lithium beam diagnostic just before and after the saddle coils have been switched on is shown in figure 16. For an otherwise identical discharge where the configuration of the saddle coils has been rotated by 90° the shift of the perturbed separatrix and correspondingly the shift in the density profile goes in the opposite direction.

Figure 17 shows edge density profiles from the Li-beam and Thomson scattering

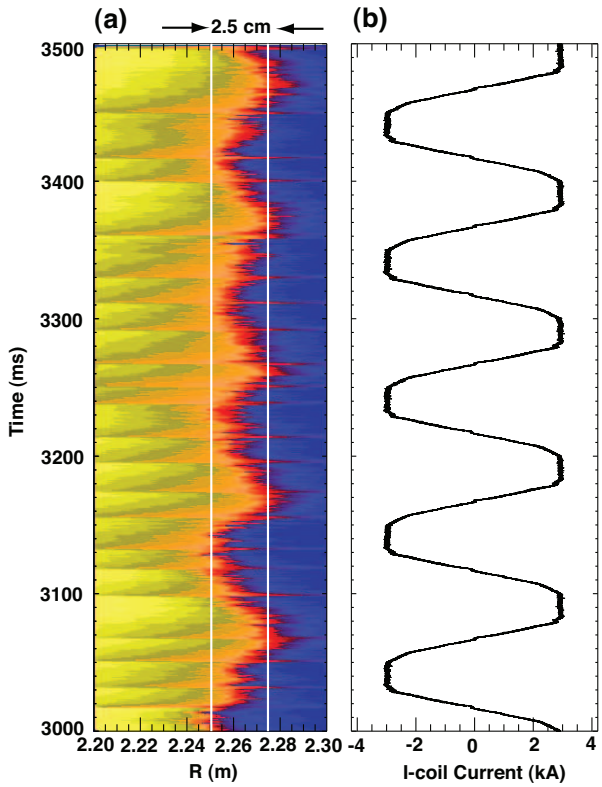


**Figure 15.** (a) Colour contour plot of the variation in the LFS edge electron density $n_e$ measured by profile reflectometry versus time and major radius $R$ at an elevation of $z = 0.05$m. (b) $n = 2$ RMP coil current in the upper 210° segment showing the rotating $n = 2$ RMP for reference.

diagnostics mapped onto the poloidal flux radius $\rho_{pol}$. Whereas the mapping is good without RMPs, the profiles from the two diagnostics seem to be shifted apart when the coils are switched on. This is mostly due to the fact that the toroidal positions of the two diagnostics differ by 137° and see a different shift of the perturbed separatrix, in this case outward for the Li-Beam and inward for the Thomson scattering diagnostic. The displacement between these two sectors, which should see the maximum displacement for an $n = 2$ field, is only ±3mm, which is equivalent to 0.6% of the minor radius [4], significantly less than in other devices.

A similarly negligible displacement is observed in NSTX when an $n = 3$ RMP is applied from the ex-vessel coils [39], as seen in figure 18. Here, the electron density and temperature profiles are shown (averaged for many time slices both with and without RMPs applied) as measured by the Thomson scattering diagnostic.

Overall, there are a wide range of the displacements observed in different machines: NSTX and ASDEX Upgrade observe sub-cm displacements for all configurations of applied fields. In contrast, MAST, DIII-D and JET can measure significant displacements, up to ±3.5% of the minor radius when the field is resonant. Furthermore, the amplitude, and even the direction of the boundary displacement is sensitively

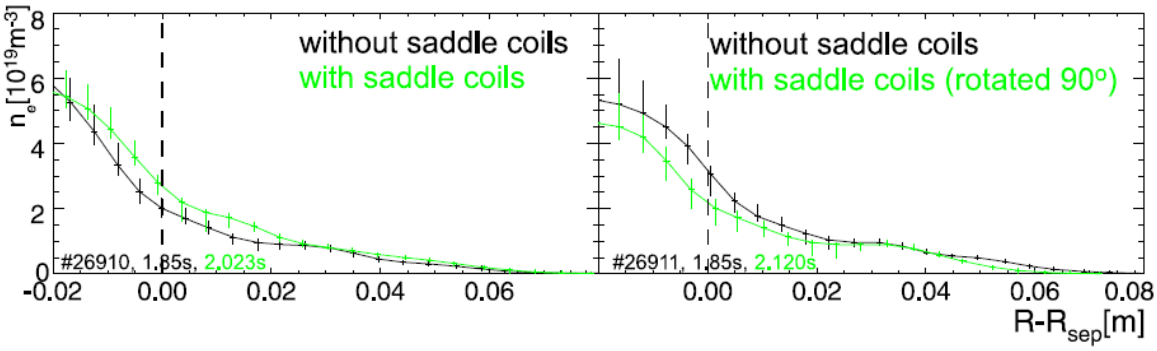


**Figure 16.** Density profiles from the lithium beam as a function of the distance to the unperturbed separatrix at the height of the beam at time points between ELMs shortly before (black) and after (green) switching on the saddle coils. The two pictures show shots with the magnetic perturbation rotated by 90°.

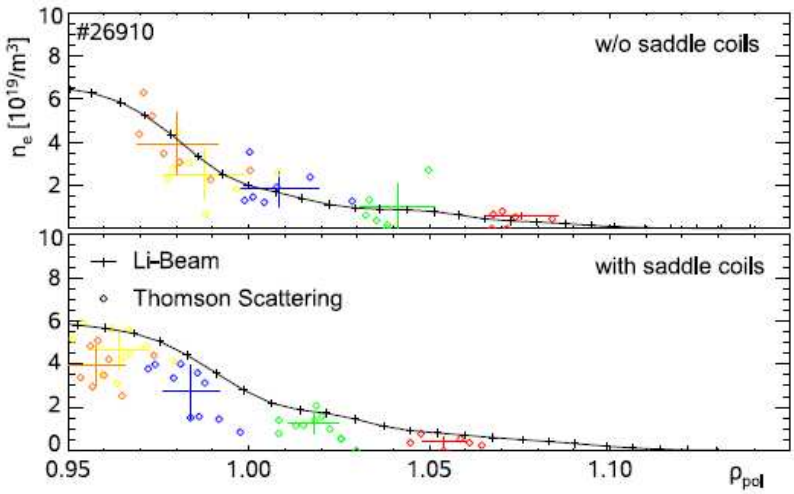


**Figure 17.** Mapping of the density measurements from Li-Beam (black) and Thomson-Scattering (coloured, each colour denotes one channel) on the normalised poloidal flux radius. Thomson Scattering measurements are averaged over 100ms, only using time points between ELMs.

dependent upon the interaction of the plasma response to the applied non-axisymmetric field with the radial position feedback of the plasma control system.

### *4.1. Multi-machine Database*

In order to compare the measurements of non-axisymmetric displacements made in different machines, a multi-machine database has been established, incorporating data from 30 discharges from 5 different machines. The database contains information on $I_p$, $B_t$, $R_0$, $a$, $q_{95}$, $n_{e,ped}/n_{GW}$, $\beta_N$, $b^r_{res}$ and the measured displacement. There is a very weak correlation between the displacement and all other parameters except for the

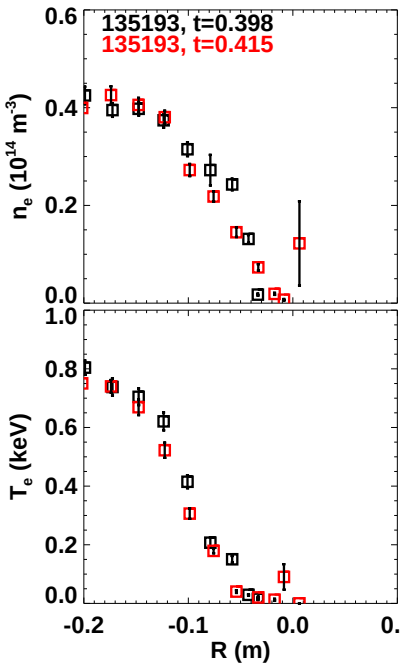


**Figure 18.** Thomson scattering measurements of the electron density and temperature profiles in NSTX with and without an $n = 3$ applied RMP, showing negligible displacement caused by the RMP.

resonant applied field. For this study, a universal definition of the resonant field is used. Here, $b^1$ represents the normalised component of the perturbed field perpendicular to equilibrium flux surfaces and is given by $b^1 = (B \cdot \nabla\psi_{pol}^{1/2})/(B \cdot \nabla\phi)$ where $B$ is the total field vector and $\phi$ is the toroidal angle [38]. The effective radial resonant field component of the applied perturbation normalised to the toroidal field ($b_{res}^r$) is the amplitude of the resonant Fourier component in the spectrum of $b^1$ divided by the average value of $\nabla\psi_{pol}^{1/2}$ on the magnetic surface, normalised to the major radius (see page 47 of reference [38]):

$$b_{res}^r = 2|b_{m,n}^1|R_0\langle\nabla\psi_{pol}^{1/2}\rangle \tag{1}$$

Figure 19 shows the strong linear correlation between the measured 3d displacement (here averaged between all toroidal positions with highly spatially resolved data, removing of course the expected null points) and the resonant field as defined in equation 1. This implies that whilst the vacuum modelling cannot give an accurate determination of the amplitude of the 3d displacement, it does give a qualitative prediction on the variation of the 3d corrugation with respect to the plasma parameters or the configuration of the applied non-axisymmetric fields. Finally, it is worth noting that there is a very weak correlation between the measured displacements and the normalised pressure in this database. Whilst this suggests that plasma response is not a leading order parameter in determining the displacements across this multi-machine

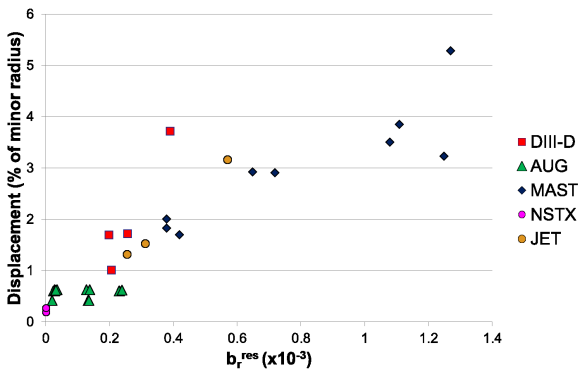


**Figure 19.** The RMP-induced displacement as a fraction of the minor radius as a function of the resonant applied field at the last rational surface as defined in ERGOS for a multi-machine database covering a wide range of $q_{95}$, $n$, $\beta_N$ and resonance.

database, it should be noted that a more appropriate parameter would be $\beta_N/\beta_N^{no-wall}$, which might be expected to determine the expected plasma response more than the absolute pressure.

At the resonant field expected in ITER, this linear fit would give an empirical scaling for the displacement in ITER of $\pm 2.25\%$ of the minor radius, equating to 9cm peak-to-peak. This means that if the plasma control system were to exacerbate the displacement and apply an $n = 0$ correction to the $n = 3$ or $n = 4$ corrugation, the displacement of the boundary would exceed the limits expected for reliable RF heating coupling and even for heat loads on the plasma facing components. This is far from a robust prediction, but nonetheless, exemplifies why this could be a concern for ITER operation.

## 5. Modelling of displacements due to RMPs in present machines

The range of displacements observed in present-day machines presented in section 4 have been modelled using a range of numerical modelling tools – (1) vacuum field line tracing codes giving the change in the position of the magnetic boundary, which is represented by the difference in position of the stable and unstable manifolds when RMPs are applied; (2) ideal three dimensional equilibrium codes, which do not solve the Grad-Shafranov equation, but instead perform an energy-minimisation procedure to find an equilibrium state, though the codes used in this study assume ideal, nested flux surfaces; (3) nonlinear MHD codes, which can capture the screening of the applied field, the response of the plasma, the effects of plasma rotation and an X-point geometry. All these models, with very different approaches and different approximations, have been compared to different machine data in different parameter space with varying levels of success, illustrating that extrapolation of the 3d corrugation likely in ITER when RMPs are applied is a complex problem.

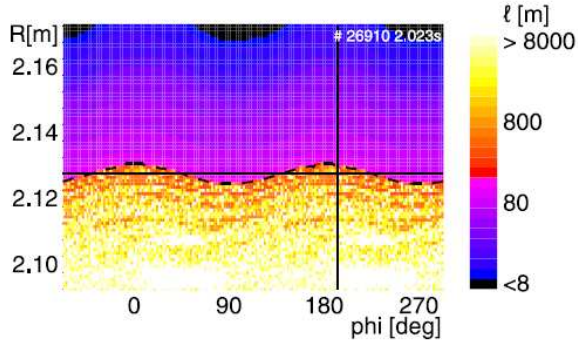


**Figure 20.** The plasma boundary predicted by the a field line tracing calculation as a function of toroidal angle for ASDEX Upgrade shot 26910 with an $n = 2$ RMP applied, showing the perturbed boundary compared to the position of the separatrix before RMPs are applied (solid black line). Connection length to the low field side target for field lines starting at a horizontal plane at $z = 0.326$m (height of the lithium beam) around the torus. Marked are the position of the lithium beam at 193° and the unperturbed separatrix at R=2.125m. The dotted line marks the position of the 'perturbed separatrix'.

### *5.1. Vacuum field line tracing*

The simplest prediction for a boundary corrugation comes from vacuum field line tracing, ignoring the plasma response and the shielding of the applied field, which have been shown to be important for understanding ELM behaviour in the presence of RMPs, but at the same time, have also given a reliable prediction for strike-point splitting on the divertor plates, indicating that they are reliable in the scrape-off layer and right at the plasma edge at least. To some extent, the applicability of vacuum modelling is also confirmed by figure 19 which shows a strong correlation between the resonant field given with vacuum modelling and the measured corrugation of the plasma boundary across 5 different machines. Figure 20 shows a laminar plot illustrating the connection length of field lines from a vacuum field line tracing calculation with an $n = 2$ RMP applied in ASDEX Upgrade [4]. The dashed black line is an effective plasma boundary, marking the envelope of the stable and unstable manifolds, which can be compared to the solid black line marking the position of the axisymmetric separatrix. There is a toroidal corrugation, though it is only ±3mm, which agrees well with the sub-cm boundary displacement observed experimentally, as seen in figure 16.

In order to confirm this prediction, another independent vacuum field line calculation has been performed with the ERGOS code [38] for ASDEX Upgrade shots with different resonant field strength at the last rational surface. Figure 21 shows the plasma boundary prediction in a laminar plot produced by ERGOS when either even parity of odd parity $n = 2$ RMPs are applied. For this equilibrium, the even parity case is well aligned with the equilibrium q-profile, as evidence by the larger corrugation amplitude, though in both cases the displacements are predicted to be sub-cm, in line

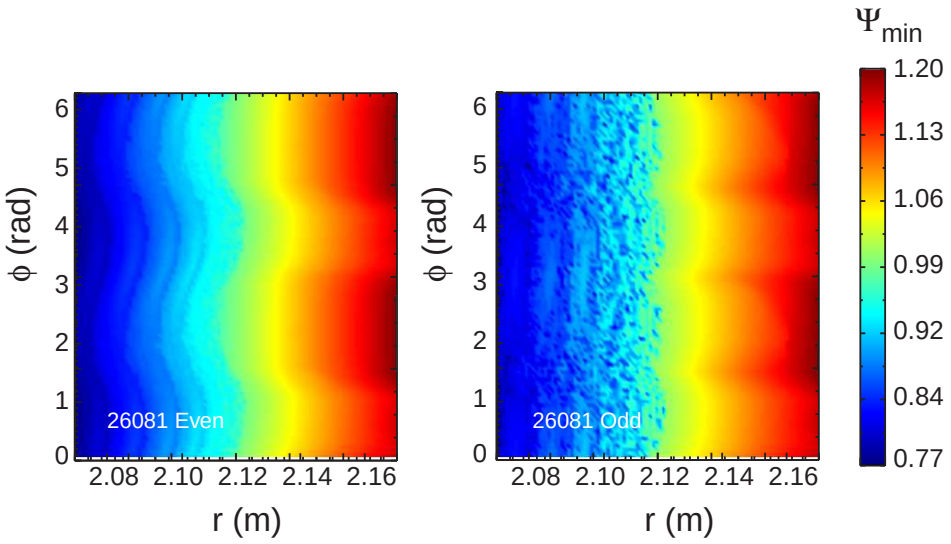


**Figure 21.** The plasma boundary predicted by the ERGOS code as a function of toroidal angle for ASDEX Upgrade shot 26081 when either (left) even parity or (right) odd parity $n = 2$ non-axisymmetric fields are applied

with figures 20 and 16.

However, there are examples where vacuum modelling somewhat under predicts the displacements seen experimentally. For instance, the displacements seen when rotating $n = 2$ RMPs are applied in DIII-D are compared to predictions from the TRIP3D-MAFOT vacuum magnetic field model in figure 22 [43]. The vacuum modelling predicts only $\pm 2.5$mm displacement whereas the BES measurements give $\pm 0.8 - 1.2$cm, representing a factor of 4-5 times larger than the vacuum prediction. Whilst the vacuum prediction does not include any screening effects, it also neglects the amplification from the plasma response, which seems to be important in this case. It is shown later that these DIII-D measured displacements are replicated by a nonlinear MHD model which incorporates such plasma amplification effects [44].

A similar under prediction of the boundary corrugation is given by vacuum modelling of MAST discharges with an $n = 3$ RMP applied. Figure 23 compares a laminar plot from ERGOS vacuum modelling from which the vacuum prediction of the displacement can be inferred, compared to the measured displacement observed on the Thomson scattering diagnostics for an $n = 3$ even parity applied field. The experimental measurements show a boundary shift of $\pm 2.5$cm, which is a factor of four larger than the vacuum prediction of $\pm 5 - 6$mm [6].

This indicates that vacuum modelling predicts the edge displacement in ASDEX Upgrade accurately, but cannot explain the larger displacements observed in MAST. In order to compare these cases directly, the resonant field in the two machines is compared using the same vacuum field line tracing code, ERGOS, as shown in figure 24. It is evident that the application of $n = 6$ RMPs in MAST leads to a factor of five larger local resonant field than the $n = 2$ field applied in ASDEX Upgrade. This

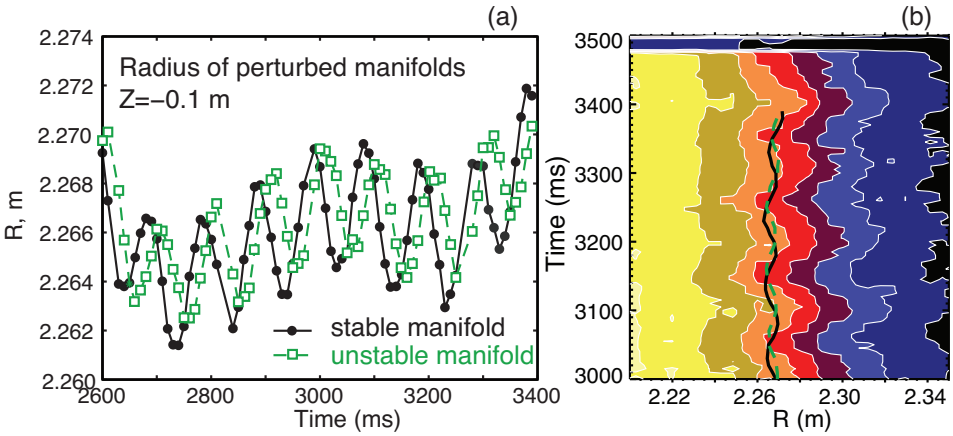


**Figure 22.** (a) Temporal evolution of the major radius $R$ of the (filled black circles and solid black line) stable and (open green squares and green dashed line) unstable manifolds at an elevation of $z = -0.1$m on the LFS midplane computed by the TRIP3D-MAFOT vacuum magnetic field model (no plasma response). Each manifold is displaced by 4-5mm over a cycle of the $n = 2$ RMP rotation. (b) Colour contour plot of the beam emission intensity at an elevation $z = -0.1$m versus $R$ and time in the LFS boundary, showing the displacement in the beam emission profile. The measured BES displacement is compared with the major radius R of the (black solid line) stable and (green dashed line) unstable manifolds at an elevation of z = -0.1m that result from the splitting of the divertor separatrix due to the non-resonant interaction with the $n = 2$ magnetic perturbation. The BES displacement of 1.8-2.4 cm over 18 cycles of the $n = 2$ rotation is $4-5$ times the predicted vacuum magnetic field model displacement.

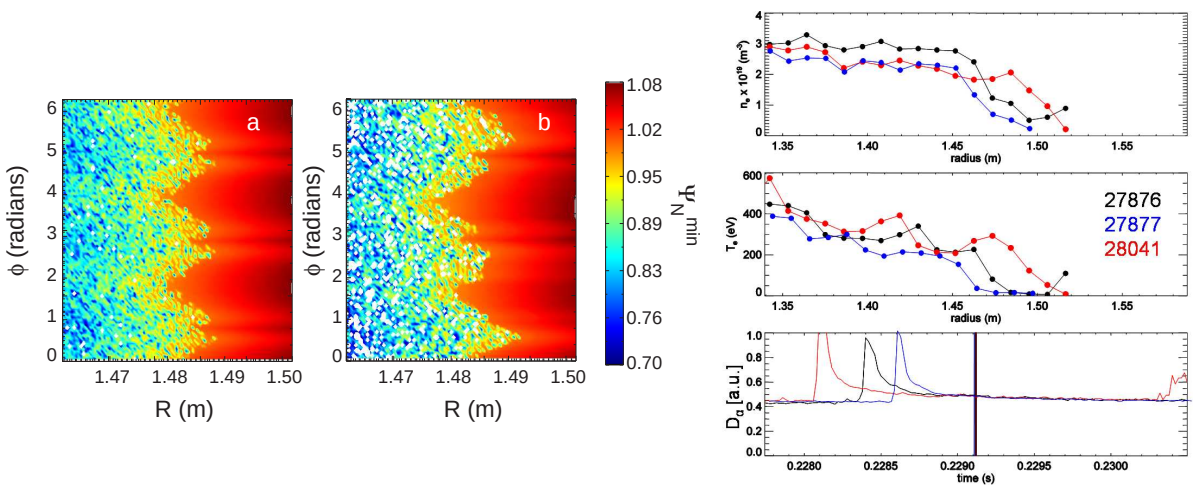


**Figure 23.** (left) A laminar plot showing the deformation of the 'boundary' in MAST when an $n = 3$ RMP is applied as predicted by ERGOS is $\pm 5 - 6$mm, which is significantly less than the displacement measured experimentally, for instance (right) on the Thomson scattering diagnostics, where a displacement of $\pm 2.5$cm is observed when the RMPs are switched on.

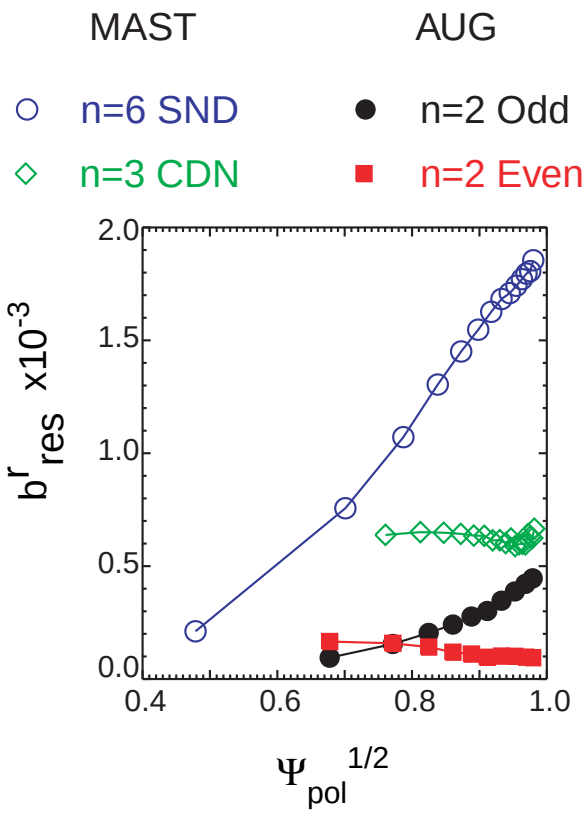


**Figure 24.** The resonant component of the applied magnetic field as a function of the minor radius as predicted by the ERGOS vacuum field line following code for MAST plasmas with $n = 3, 6$ RMPs applied compared to ASDEX Upgrade plasma with $n = 2$ field applied with either odd or even parity.

larger resonant field partially explains why the MAST plasmas experience larger edge corrugations, though the underprediction afforded by vacuum modelling in figure 23 suggests that there is a plasma amplification of the applied field as well.

### *5.2. Ideal three dimensional equilibrium reconstruction*

The next level of complexity in modelling 3d displacements is ideal 3d equilibrium reconstruction. Sub-0.01$a$ displacements of the plasma boundary observed experimentally are also replicated using such 3d equilibrium modelling in both ASDEX upgrade and in NSTX. Figure 25 shows the toroidal dependence of the position of the plasma boundary predicted by the VMEC 3d equilibrium code when an $n = 3$ RMP is applied in NSTX [39]. It is evident that the boundary is expected to be perturbed by only $\pm$1mm, in good agreement with the measured invariance of the pedestal foot position seen in figure 18.

Three dimensional ideal equilibrium calculations also give good agreement with experimental cases where larger boundary perturbations are observed. Figure 26 shows STELLOPT predictions for the plasma boundary displacement as a function of toroidal

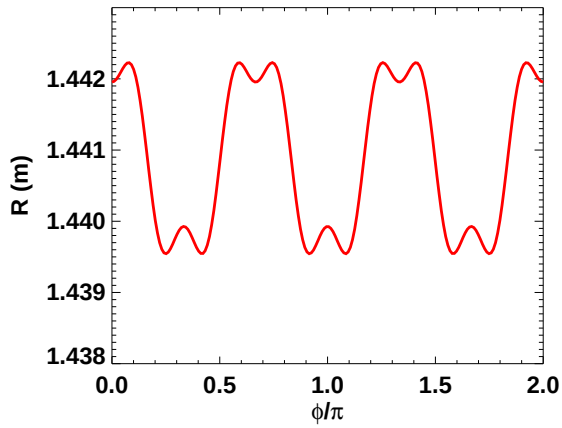


**Figure 25.** The toroidal dependence of the plasma boundary as predicted by VMEC when an $n = 3$ RMP is applied in NSTX.

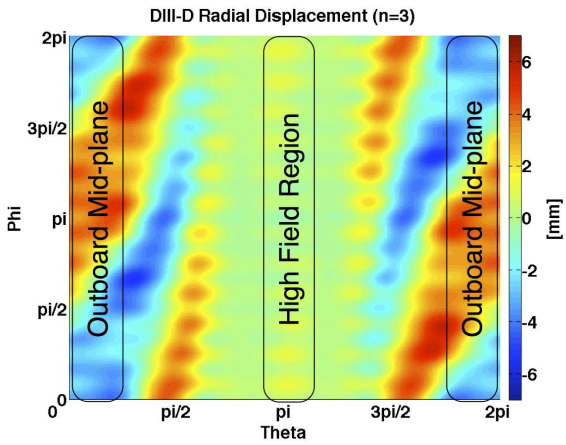


**Figure 26.** The plasma boundary displacement as a function of toroidal and poloidal angles as predicted by the STELLOPT code for a DIII-D plasma with an $n = 3$ RMP applied.

and poloidal angles in a DIII-D plasma when an $n = 3$ RMP is applied. The STELLOPT code [45] is designed to optimise the VMEC 3D MHD equilibrium to a set of target physics parameters derived from different plasma diagnostics. The reconstruction predicts a boundary corrugation of ±6mm, maximised on the low-field side midplane, in good agreement with measured displacements [46].

Ideal 3d equilibrium reconstruction has also been applied for MAST plasmas when RMPs are applied. Figure 27 shows the outboard midplane radial position of the last closed flux surface predicted by VMEC when an $n = 3$ RMP is applied to a connected double-null MAST plasma where ELM mitigation is observed [47]. Without an applied $n = 3$ field, there is a natural $n = 12$ boundary corrugation associated with the toroidal field ripple, though this is ±2mm, below the resolution of any diagnostic. However,

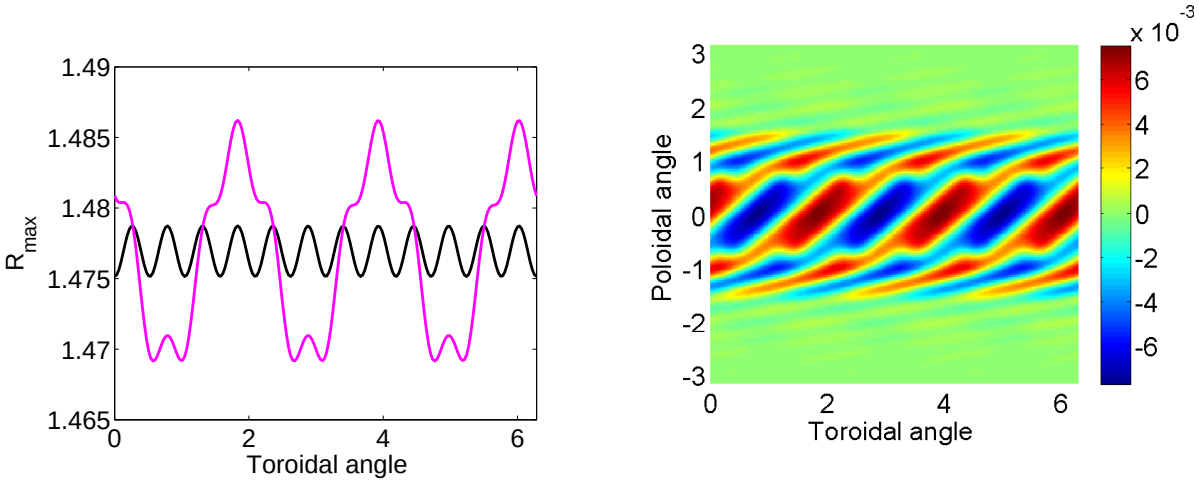


**Figure 27.** (left) The plasma boundary predicted by VMEC for a MAST connected double null plasma when an n=3 RMP is applied (pink) compared to the case with no RMP but with toroidal field ripple (black). (right) The boundary displacement predicted by VMEC as a function of toroidal and poloidal angle, showing maximum displacement on the midplane for this double-null plasma.

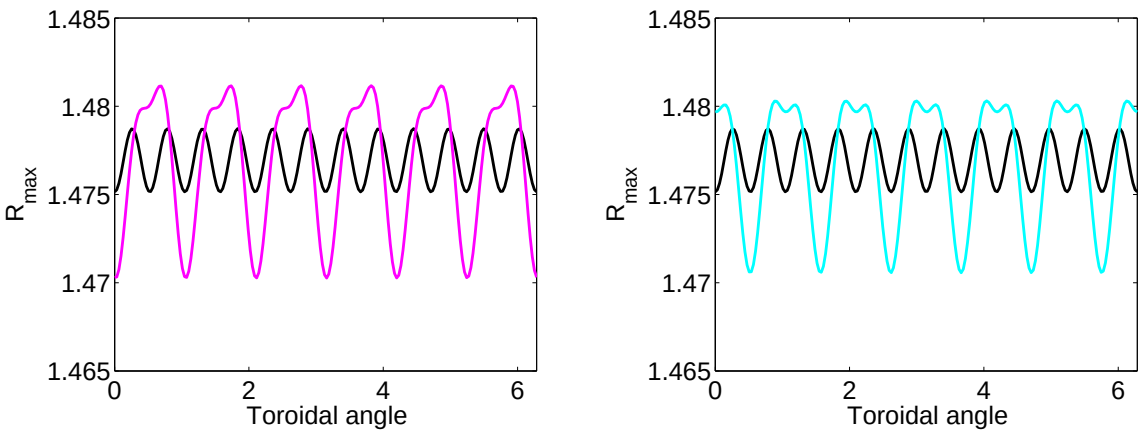


**Figure 28.** The plasma boundary predicted by VMEC for a MAST connected double null plasma when an n=6 RMP is applied compared to the case with no RMP but with toroidal field ripple when the RMP has (left) even parity configuration and (right) an odd parity configuration.

when an $n = 3$ field is applied, there is a clear edge corrugation of $\pm 7$mm, which is maximised at the midplane.

This can be compared to the edge corrugation predicted by VMEC when an $n = 6$ RMP is applied to a connected double null MAST plasma, as shown in figure 28. It is evident that the $n = 6$ RMPs produce slightly smaller, but still significant, edge displacements of $\pm 5$mm. In both of these cases, the fields are not optimally aligned to the plasma equilibrium.

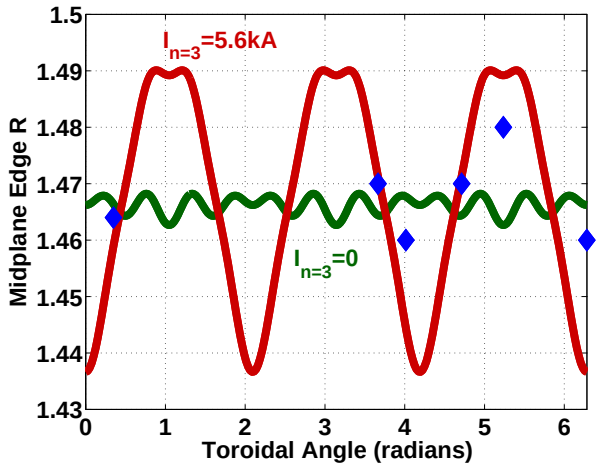


**Figure 29.** The plasma boundary displacement as a function of toroidal angle as predicted by the ANIMEC code compared to measurements of the midplane displacement in MAST when an $n = 3$ RMP is applied.

When the applied field is optimally aligned with the plasma field– at which point the ELM mitigation is maximised [47] – the corrugation is even larger. Figure 29 shows ANIMEC modelling of a MAST connected double null plasma when an $n = 3$ field is applied with a pitch angle to align the field with the $q$-profile. In this case the edge corrugation is $\pm 2.5$cm, equating to $\pm 4.5\%$ of the minor radius. Also shown in figure 29 are data from different diagnostics in MAST when this phase of $n = 3$ RMP is applied, showing excellent agreement between the measured position of the plasma boundary and the predicted edge position from ANIMEC, suggesting that ideal 3d MHD equilibrium reconstruction is able to replicate the experimental shifts observed in MAST accurately.

However, there are examples where ideal 3d equilibrium reconstruction does not replicate the large boundary corrugations observed in some experiments. For instance, figure 30 shows VMEC 3d reconstruction of the JET plasma with 80kAt in the external coils producing an $n = 2$ field. This $n = 2$ RMP is observed to produce a boundary displacement of $\pm 3$cm [36], whereas VMEC predicts only a $\pm 1$cm boundary corrugation for this plasma equilibrium.

### *5.3. Resistive MHD modelling*

Similarly, it can be seen by comparing figure 26 with figures 14 and 15 that the STELLOPT 3d equilibrium reconstruction produces slightly smaller displacements at the boundary than those which are measured experimentally in DIII-D (though it is worth noting that it produces a much better agreement than the factor of four discrepancy with vacuum modelling seen in figure 22). The next level of complexity is to use a resistive MHD model which allows for the plasma response to the applied field, allowing amplification by marginally stable MHD modes as well as screening of the field. Figure 31 shows such a comparison between the electron temperature pedestal measured

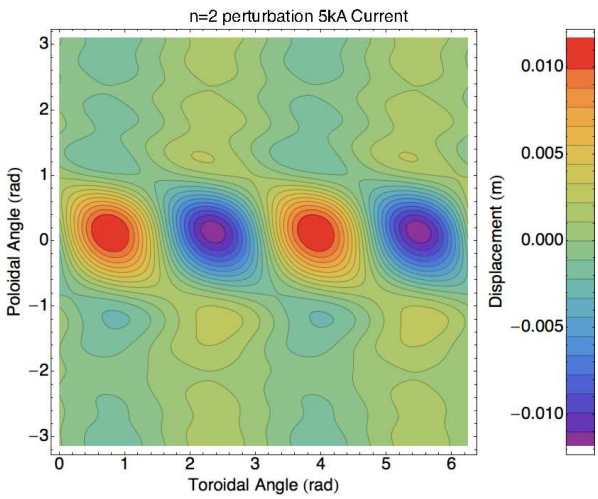


**Figure 30.** The plasma boundary displacement as a function of toroidal and poloidal angles as predicted by the VMEC code when an $n = 2$ RMP is applied in JET.

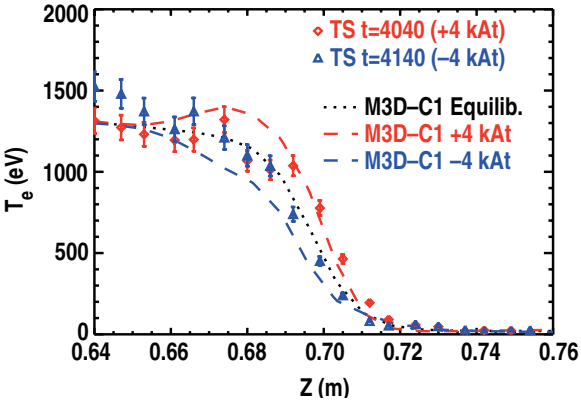


**Figure 31.** The electron temperature profile as a function of $Z$ as measured by the Thomson scattering diagnostic in DIII-D (symbols) compared to the prediction from the M3D-C$^1$ linear MHD code for two phases of an applied $n = 3$ RMP, showing good agreement and a clear edge displacement.

by the Thomson scattering diagnostic in DIII-D and that predicted by the M3D-C$^1$ MHD code. In this case, the displacements observed experimentally are accurately modelled by linear resistive MHD.

Furthermore, M3D-C$^1$ is also able to replicate the dependence of the corrugation amplitude on plasma parameters. In DIII-D, larger displacements are observed at larger $q_{95}$: plasmas with $q_{95} = 3.1$ have $\xi_a \approx 4$mm whereas plasmas at $q_{95} = 3.8$ have $\xi_a \approx 8$mm. Such a dependence on plasma current is replicated by M3D-C$^1$ as shown in figure 32. This trend follows the vacuum field intuition, since $I_{RMP}/I_P$ increases with $q_{95}$, here changed by scaling the current. Indeed, vacuum modeling based on these shots recovers this trend [48]. It is contrary, however, to the intuition one might apply if plasma

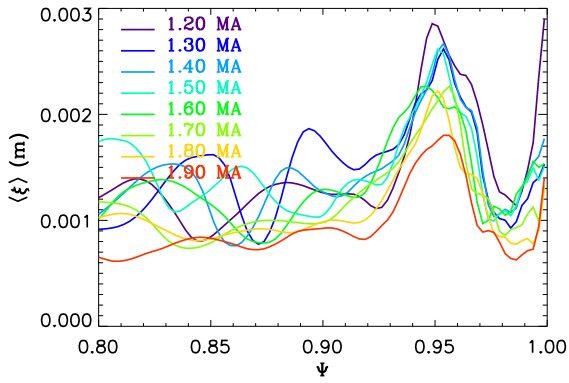


**Figure 32.** The flux surface perturbation as a function of radius for different values of plasma current with an applied $n = 3$ RMP, as modelled by linear M3D-C$^1$ runs. It is clear that the edge displacement increases for lower $I_p$, that is to say for higher $q_{95}$ in this case.

amplification plays a key role in determining the edge displacement. One might assume that higher current sustains higher pressure gradient, making edge modes more unstable, hence amplifying the applied field and leading to *larger* displacements, rather than the smaller edge corrugation observed. However, resistive MHD including rotation is able to capture both amplification and screening and as such includes the pertinent physics to allow good agreement across a wide range of plasma conditions.

The simulations in figures 31 and 32 use a linear MHD approximation. Here we consider linear modelling as appropriate provided $|\mathrm{d}\xi_r/\mathrm{d}r| < 1$. If this condition is not met, then the flux surface displacements overlap, implying a breakdown of the condition $B \cdot \nabla T_e = 0$. In order to verify the applicability of the linear model in these conditions, the displacements predicted using linear MHD have been compared to non-linear simulations, as shown in figure 33. The overlap criterion that $|\mathrm{d}\xi_r/\mathrm{d}r| < 1$ is clearly met across the whole minor radius, and commensurately, the boundary displacements, and indeed the whole pedestal electron temperature profile, is in good agreement in the linear and nonlinear simulations.

Another nonlinear resistive MHD code, JOREK [49], has been used to simulate MAST and JET plasmas when RMPs are applied. Figure 34 shows the pedestal electron density and temperature profiles with and without an $n = 3$ RMP applied in different toroidal positions in MAST. Two things worth noting are that when the RMPs are applied both the density is more degraded than the temperature, and that there is a clear toroidal nonaxisymmetry to the boundary position. This is also seen in the Poincare plot of the magnetic surfaces, where a midplane displacement of $\pm 7 - 8$mm is predicted by JOREK, with even larger displacements observed near the X-point. However, it should be noted that these simulations do not include experimentally relevant flows, and the applied field is an order of magnitude smaller than in the experiment, presumably since the absence of realistic flows precludes the screening that exists experimentally. This is

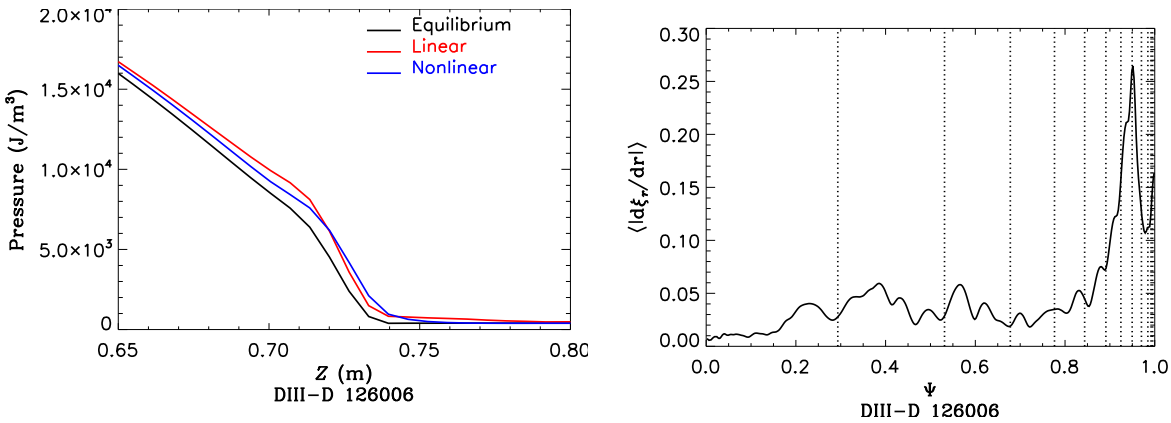


**Figure 33.** The plasma electron pressure as a function of vertical position (along the line of sight of the Thomson scattering) in DIII-D as predicted by the M3D-C[1] code, comparing the results of linear and non-linear simulation when an $n = 3$ RMP is applied.

therefore not intended as a comparison between experiment and simulation.

In contrast, JOREK simulations with realistic resistivity and flows have been performed for JET discharges with an $n = 2$ RMP applied. For discharge 77329, the measured displacement resulting from the application of the $n = 2$ RMP is $\pm$1cm. Figure 35 shows the predicted displacements at the plasma top, X-point and midplane respectively when JOREK is run without realistic diamagnetic and toroidal flows included. In this case the boundary displacement is $\pm$1.2cm. When realistic flows are included in the simulation, the boundary displacement is halved, to $\pm$6mm, as shown in figure 36.

In section 4 the range of measured displacements in present day machines was detailed, ranging from $\pm$3.5% of the minor radius to negligible edge corrugation. In a similar vein, the models needed to replicate the experimental observations range from simple vacuum field line tracing, to ideal 3d equilibria and nonlinear resistive MHD simulations. Whilst there is a strong correlation between the resonant field predicted by vacuum models and the measured displacement, seen in figure 19, vacuum modelling does not always accurately replicate the absolute magnitude of the empirical observations, even if it does provide qualitative trends with respect to the plasma parameters. Indeed, in all cases where large displacements are observed, either ideal 3d equilibrium reconstruction (in MAST) or resistive MHD including plasma amplification effects (in DIII-D and JET) are required to replicate the observations. However, there remains uncertainty in any of the models, in the level of plasma and rotation screening of the applied fields, on the damping caused by the applied field and the nonlinear interaction of 3d fields, marginally stable modes and rotation, and therefore it is prudent to use all models available and take the worst case scenario when making ITER predictions, as follows in section 7.

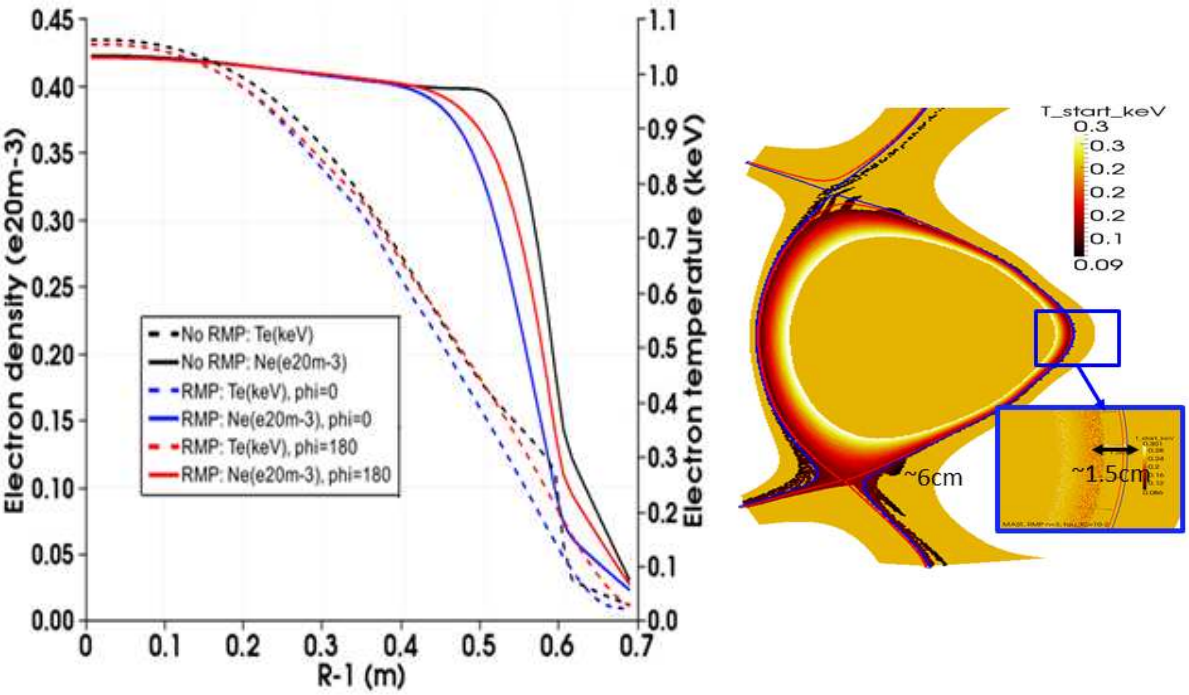


**Figure 34.** (left) The plasma electron temperature and density modelled by JOREK as a function of the radius across the pedestal region for MAST when RMPs are applied (at only an order of magnitude less than the experiment, but without diamagnetic or toroidal flows) showing a clear degradation of the pedestal and toroidal asymmetry; (right) The Poincare plot of the equilibrium modelled with JOREK, showing 1.5cm displacement on midplane, and even larger shifts near the X-point.

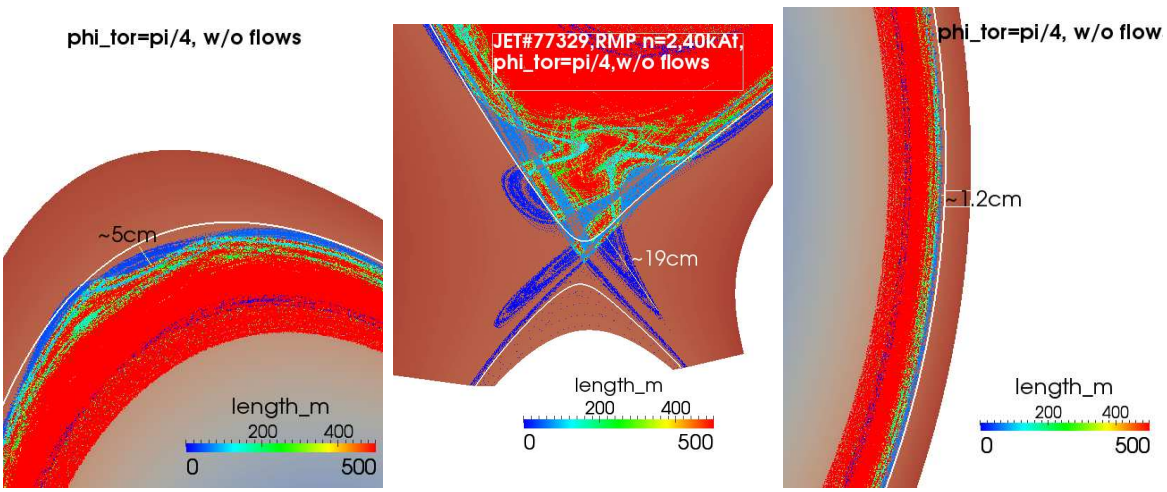


**Figure 35.** Poincare plots showing the (left) top, (middle) lower X-point region and (right) midplane of JET discharge 77329 modelled using JOREK without realistic diamagnetic and toroidal flows included.

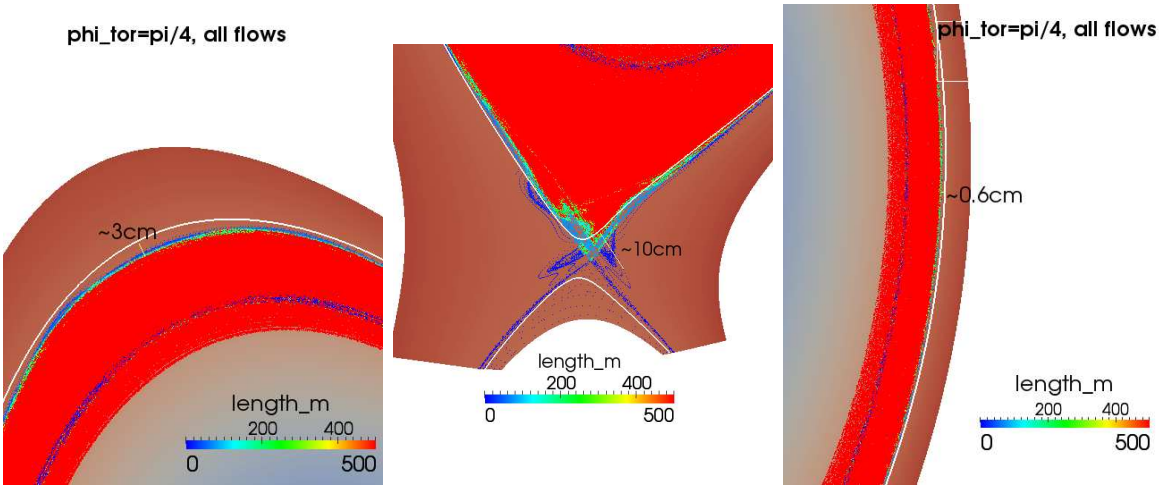


**Figure 36.** Poincare plots showing the (left) top, (middle) lower X-point region and (right) midplane of JET discharge 77329 modelled using JOREK when realistic diamagnetic and toroidal flows are included.

## 6. Modelling of displacements due to core MHD in ITER

As discussed in section 2, the plasma scenario which is most prone to long-lasting saturated MHD is the so-called 'hybrid' or advanced inductive scenario due to the broad, low shear region in the $q$-profile. Of course, the baseline scenario is expected to experience MHD instabilities in the core, notably sawtooth oscillations, which could give rise to neoclassical tearing modes, both of which can lead to displacements of the plasma boundary. However, in the case of sawteeth the displacements are small and transient, and for NTMs the confinement degradation is a much more serious issue than whether the boundary is deformed. In comparison, the saturated core MHD experienced in hybrid plasmas is usually not overtly detrimental to the plasma performance, but can last for many energy confinement times, and can lead to enduring displacements of the boundary which could result in difficulties for the plasma control system or for cycling of heat loads on plasma facing components. Therefore, it is the boundary corrugation experienced in the ITER hybrid scenario which we analyse numerically in this section.

Figure 37 shows the pressure, current density and $q$ profiles assumed in the modelling of ITER with the Animec 3d equilibrium code. The current density profile has been tailored in order to give a slightly reversed shear safety factor profile, though actually, the reverse shear is not a strong constraint on the results presented here and qualitatively similar results would be obtained for a flat, low-shear profile provided $q_{min} \approx 1$. Different bootstrap assumptions have been made to generate equilibria with either (i) high pressure gradient and bootstrap current, (ii) lower pressure gradient and bootstrap current and (iii) high pressure gradient but small bootstrap current.

Figure 38 shows the plasma pressure for the hybrid scenario equilibrium generated by Animec for the axisymmetric branch, whilst figure 39 shows the pressure for a helical

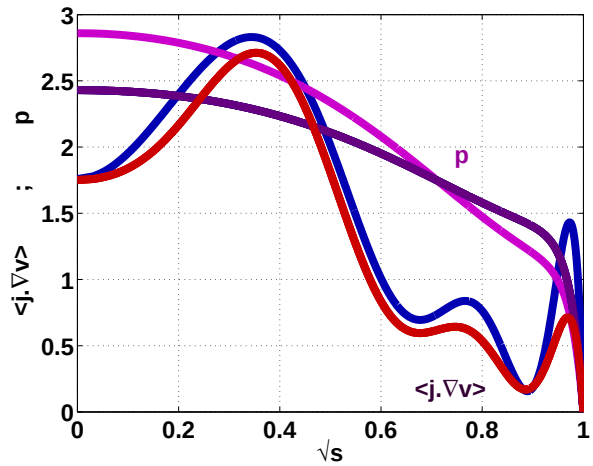


**Figure 37.** The pressure and current density profiles used for ITER hybrid scenario simulations for two cases with different assumptions for the pedestal pressure and resultant bootstrap current.

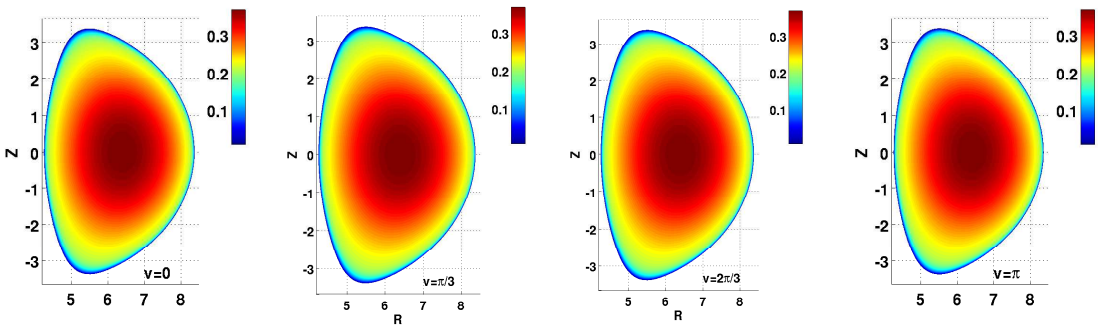


**Figure 38.** The pressure for the ITER hybrid scenario as predicted by ANIMEC for the axisymmetric equilibrium branch at $\phi = 0, \pi/3, 2\pi/3, \pi$.

core branch of the equilibrium. It is clear that although the edge flux surfaces remain the same in both cases, the plasma core can be significantly distorted when there is an $n = m = 1$ kink in the plasma core. Such a helical core would be expected to manifest itself as the long-lasting ideal perturbations observed in such 'hybrid' scenarios in MAST [10], JET [11], NSTX [13] and EAST [14].

As discussed in section 3, the absolute magnitude of the boundary displacement predicted by ANIMEC scales with the magnitude of the bootstrap current in the equilibrium. This is investigated using the profiles shown in figure 37, where it is assumed that the plasma has either (i) high pressure gradient and bootstrap current, (ii) lower pressure gradient and bootstrap current and (iii) high pressure gradient but small bootstrap current. The boundary displacement predicted by ANIMEC for each of these sets of profiles is shown in figure 40, where it is clear that including a large bootstrap current gives rise to a massive perturbation of the boundary position, with an $n = 1$ periodicity. Assuming a reduced bootstrap current, akin to that expected from

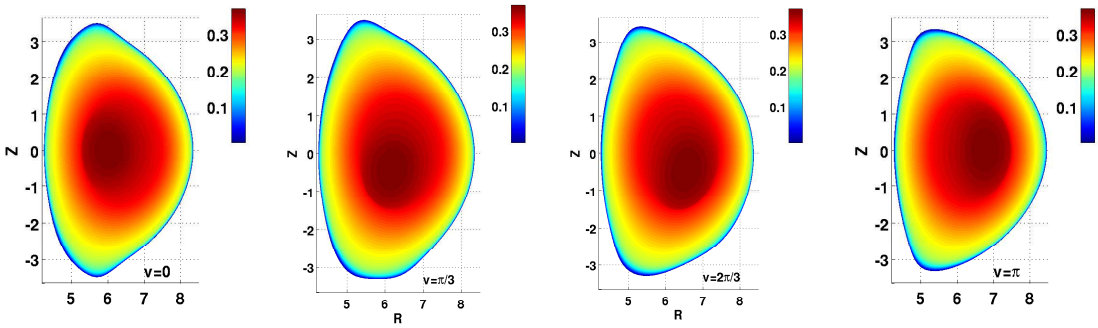


**Figure 39.** The pressure for the ITER hybrid scenario as predicted by ANIMEC for the axisymmetric equilibrium branch at $\phi = 0, \pi/3, 2\pi/3, \pi$.

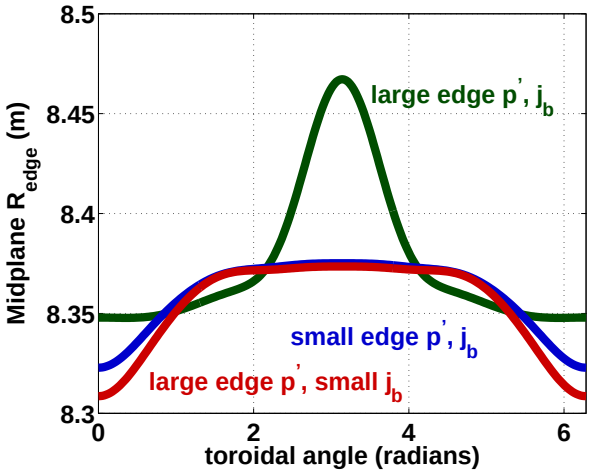


**Figure 40.** The position of the plasma boundary as predicted by ANIMEC for three ITER hybrid plasmas with either (i) high pressure gradient and bootstrap current, (ii) lower pressure gradient and bootstrap current and (iii) high pressure gradient but small bootstrap current.

neoclassical formulae [34, 35] leads to a much smaller, but still significant, displacement of ±3cm (±1.5% of the minor radius).

This boundary displacement in the presence of an $n = m = 1$ helical core is illustrated clearly in figure 41 where it can be seen that the two neighbouring states of equilibria found with ANIMEC when there is a broad low-shear region in the $q$-profile with $q_{min} \approx 1$ lead to very different toroidal dependence of the plasma boundary. In the axisymmetric equilibrium, there is no corrugation of the boundary, whereas the helical core state, which it is worth remembering is equally energetically favourable, gives rise to a ±3cm $n = 1$ distortion of the boundary.

A comparable analysis has been performed using the nonlinear MHD code, M3D-C[1]. It is worth recalling that the saturated state of an MHD instability found from an axisymmetric equilibrium is tantamount to a 3d equilibrium state for these hybrid profiles, as shown in figure 4 and reference [25]. The electron temperature perturbation

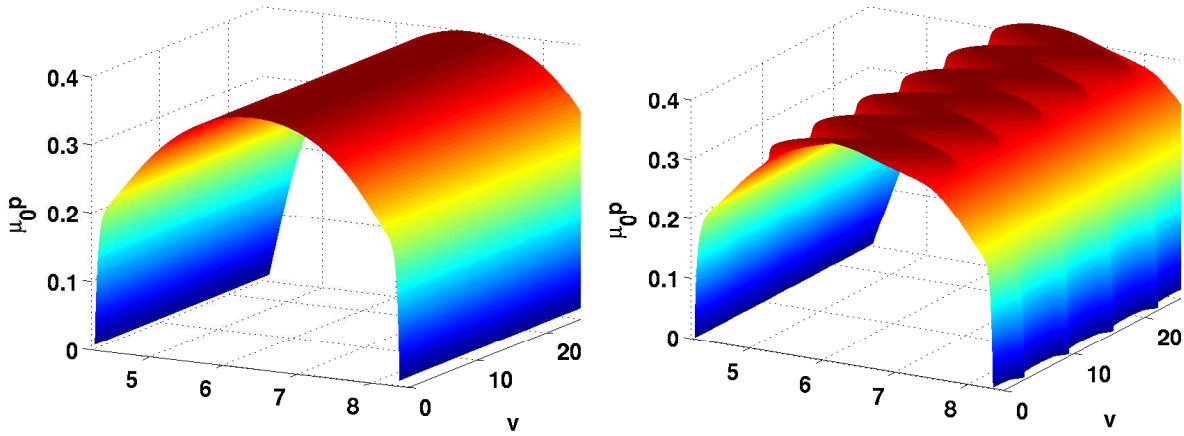


**Figure 41.** The plasma pressure as a function of radius and time, showing the $n = 1$ helical core and the perturbation to the edge position.

predicted by M3D-C[1] at different toroidal positions for the ITER hybrid scenario with realistic bootstrap current is shown in figure 42. Whilst there is a large $n = 1$ perturbation in the plasma core, there is negligible change in the position of the plasma boundary.

The fact that these two models, be it either a 3d equilibrium reconstruction using ANIMEC or a nonlinear MHD simulation with M3D-C[1], have given good agreement with measured displacements due to saturated core MHD instabilities in MAST and NSTX respectively, means that the expected displacement in ITER is highly likely to lie within the bounds of the predictions from these simulations. That is to say, the displacement in ITER hybrid scenarios due to saturated kink modes prevalent with low-shear and $q_{min} \geq 1$ is in the range $\xi_{MHD} \in \pm[0, 3]$cm, equating to $\xi_{MHD} \in \pm[0, 0.015a]$. Whilst this is not insignificant, it is within the acceptable bounds of the boundary displacement allowable in ITER for both plasma control to be effective and heat loads to the plasma facing components to be manageable.

## 7. Modelling of displacements due to RMPs in ITER

As in section 5, the displacements expected in ITER are modelled using vacuum field line tracing, ideal 3d equilibrium reconstruction and nonlinear resistive MHD codes.

### *7.1. Vacuum field line tracing*

The coil set used in these simulations is shown in figure 43, including the latest design for the in-vessel control coils (IVCCs) planned for ITER.

The TRIP3D vacuum field line tracing code has been used to predict the boundary displacement expected in a 15MA baseline scenario when full current is applied in

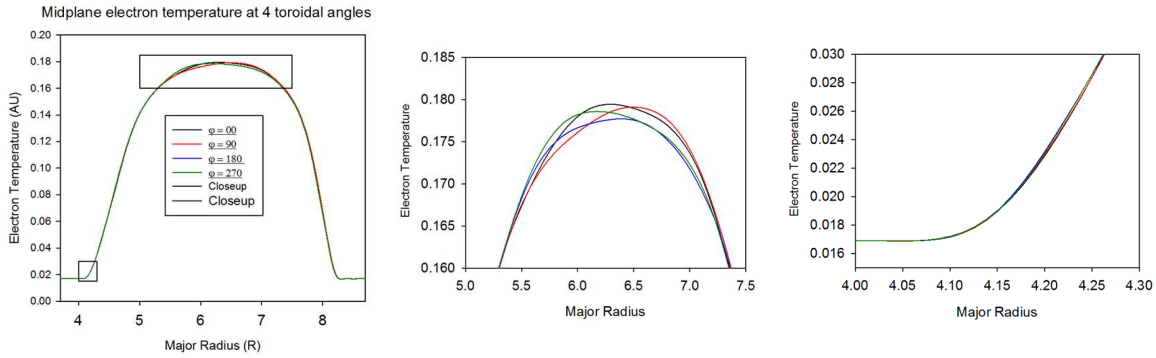


**Figure 42.** The electron temperature profile at different toroidal positions for a ITER hybrid plasma as predicted by the M3D-C[1] code for (left) the whole major radius, (centre) the core plasma showing an $n = 1$ kink mode and (right) the pedestal, showing negligible boundary displacement.

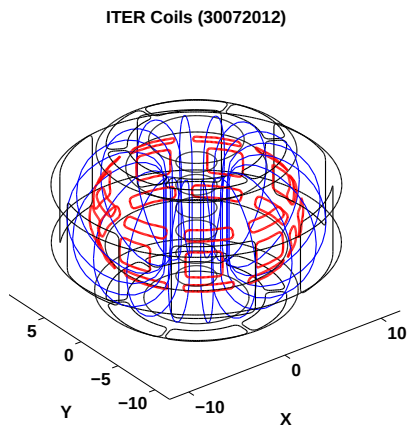


**Figure 43.** The coil set used in ITER simulations.

the IVCCs in an $n = 3$ configuration. Figure 44 shows the radial position of the axisymmetric plasma boundary in the absence of RMPs compared to the position of the unstable and stable manifolds resultant under the application of a nonaxisymmetric field perturbation. In plasma simulations one can take an isotherm or isobar as a proxy for the boundary position. The boundary location is somewhat harder to define in vacuum modelling. Non-axisymmetric magnetic perturbations split the separatrix into stable and unstable manifolds [50, 51], with corrugated structures forming where these manifolds intersect. These homoclinic tangles are computed to be particularly complex and extended near the X-point. This concept of lobe structures formed by the invariant manifolds of the perturbed field has been used to explain the splitting of the divertor leg footprints observed on strike-point targets during RMP experiments [53, 54, 55, 50, 56], suggesting that at least for the boundary and scrape-off layer, vacuum modelling gives a good description of the effect of the applied fields. Nonetheless, using the difference

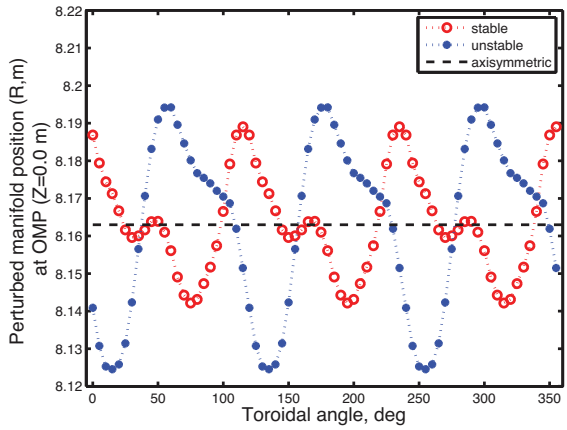


**Figure 44.** The radial position of the axisymmetric plasma boundary in ITER 15MA baseline scenario predicted by TRIP3D vacuum field line tracing code, compared to the unstable and stable manifold positions when a full-field $n = 3$ RMP is applied.

between the stable and unstable manifolds as a proxy for the boundary position, it is evident from figure 44 that simple vacuum modelling suggests a corrugation of ±3cm, representing ±1.5% of the minor radius in ITER 15MA baseline plasmas.

### *7.2. Ideal three dimensional equilibrium reconstruction*

It is possible to use a simple analytic model to find the dependence of the boundary displacement on the equilibrium $q$-profile, and thus on the resonance of the applied field. We start by taking the 3D magnetic perturbation spectrum from an M3D-C$^1$ response calculation for the baseline ITER scenario with a 3.8keV pedestal temperature and 22.5kAt in the midplane-IVCCs. The outermost radial point in the domain is chosen, at $\psi_N = 0.9988$ and $q = 4.262$. Three dimensional local equilibrium theory is used to study the sensitivity of the 3D deformation size at this surface to the local value of the safety factor. Starting with the axisymmetric flux surface shape (taken from the initial 2D equilibrium used in the M3D-C$^1$ response calculation), we add a spectrum of 3D flux surface deformations which match the 3D radial magnetic perturbation spectrum from M3D-C$^1$. We follow the procedure described in reference [40]. In the high aspect ratio, circular cross section limit the relationship between a deformation of a given helicity ($\gamma$) and the radial magnetic perturbation associated with it is given by $B_r/B_0(m,n) = (\gamma/R_0)(nq - (m-1))$, where an $m = 4$ deformation is associated with an $m = 3$ radial magnetic perturbation. With the $q$ value taken from the response calculation we find a 3D flux surface displacement at the outboard midplane of ±7mm. We then repeat the calculation of the flux surface displacement with varying safety factor, but holding the 3D perturbation spectrum fixed. The energy needed to bend equilibrium magnetic field lines decreases as we approach low order rational surfaces, therefore we find that the displacement size has a $1/x$-type sensitivity where $x$ is the

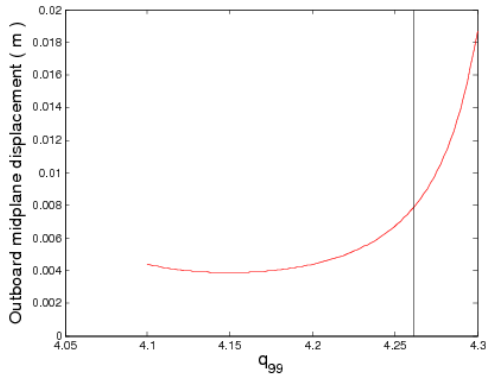


**Figure 45.** The edge displacement as a function of the edge safety factor found from simple 3d local equilibrium theory.

distance to the nearest low order rational surface. The validity of these calculations comes into question as the rational surface is approached, as the resonant component of the radial magnetic perturbation may be suppressed by flow screening, and in principle new radial perturbation spectra should be used. Here we limit our calculations to a range of $q$ values where the radial magnetic perturbation spectra used should remain valid. These calculations suggest that the displacement of the last closed flux surface will have some sensitivity to the $q$ value, as seen clearly in figure 45. Small changes in the edge $q$ value may be able to significantly modify the displacement of the last closed flux surface.

3d equilibrium reconstruction of the various ITER scenarios with either $n = 3$ or $n = 4$ RMPs applied has been performed using the VMEC code. The profiles for the baseline scenario are taken from the latest transport simulations of ITER 15MA plasmas using the CORSICA code [57]. Subtle variations in the shape – as shown in figure 46 – have also been tested, with these variations arising during the progress of this working group as the baseline scenario modelling has evolved. Whilst the difference between these two shapes is not large, the effect on the RMP-induced displacement is significant.

Figure 47 shows the boundary displacement when $n = 4$ RMPs are applied with 90kAt (the maximum allowed) in the IVCCs to the ITER 15MA L-mode (left) or H-mode flat-top (right). The maximum amplitude of the displacement is only $\pm 1.5$cm (or $\pm 0.75\%$ of the minor radius) in L-mode and $\pm 2.1$cm (or $\pm 1.05\%$ of the minor radius) in H-mode. Since the maximum displacement is off mid-plane, the values on the midplane are smaller still.

These small displacements predicted by VMEC are produced when assuming the blue shape in figure 46. When the red shape in figure 46 is assumed, the NEMEC code (a free boundary version of VMEC, which for the purposes of this study is ostensibly identical) produces much larger midplane displacements. The simulations naturally include TF ripple effects (without ferritic inserts), which alone can induce corrugations

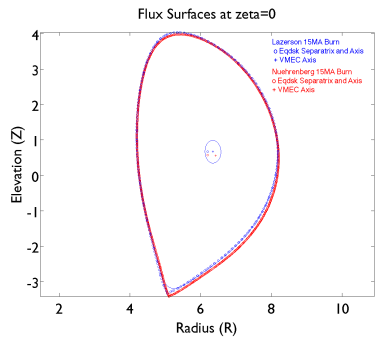


**Figure 46.** The axisymmetric plasma boundary used in free-boundary VMEC runs without RMPs applied for two variants of the ITER 15MA baseline scenario plasma.

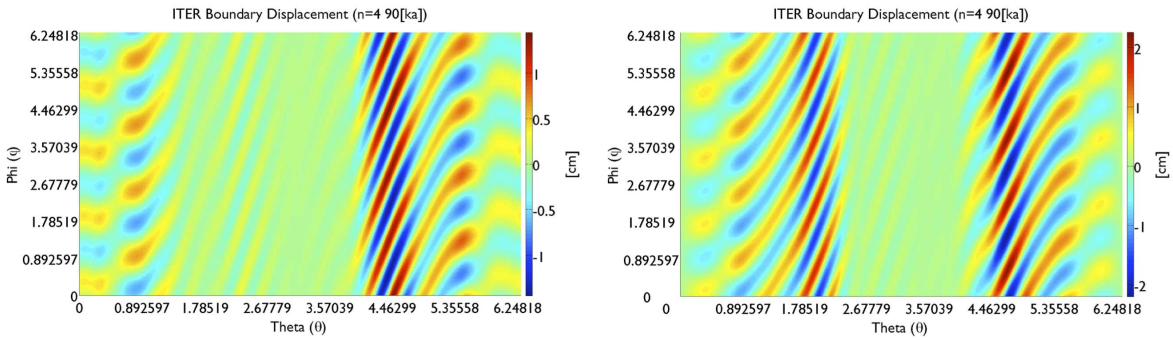


**Figure 47.** The plasma boundary displacement as predicted by VMEC for the ITER baseline scenario as modelled with CORSICA when 90kAt is assumed in the in-vessel control coils in $n = 4$ configuration for (left) the L-mode phase before burn and (right) the flat-top H-mode phase during the plasma burn.

of $\pm 7 - 8$mm. Four current distributions in the IVCCs have been studied, namely two $n = 4$ patterns with $I_{IVCC} = 90$kAt and $I_{IVCC} = 30$ kAt and two $n = 3$ patterns with $I_{IVCC} = 90$ kAt and $I_{IVCC} = 45$ kAt [58]. The $n = 4$ cases show a strong addition of $n = 5$, whilst the $n = 3$ cases have additional $n = 6$ amplitudes. In all twelve NEMEC calculations (two coil configurations $\times$ two RMP amplitudes $\times$ three plasma scenarios – 9MA flat-top, 15MA L-mode and 15MA H-mode flat-top) the outer plasma edge in the $Z = 0$ plane is displaced by several centimeters, shown in figure 48. The toroidal dependence of the displacement is not a pure $n = 3$ or $n = 4$ due to the rather unpure spectrum applied from the IVCCs together with the TF ripple. For the $n = 4$ RMPs with $I_{IVCC} = 90$kAt in the 9MA plasma, the plasma edge is displaced by up to $\approx 5$cm from its axisymmetric position. The smallest edge displacement is observed in the 15MA L-mode scenario, for both $n = 3$ and $n = 4$ RMPs, where the corrugation is roughly 1cm if $I_{IVCC} = 90$kAt. Pertinently, the 15MA cases with $I_{IVCC} = 90$kAt in $n = 4$ configuration has a midplane displacement of $\pm 2$cm (or $\pm 1\%$ of the minor radius), which is significantly larger than that shown in figure 47 when a slightly different plasma shape is assumed.

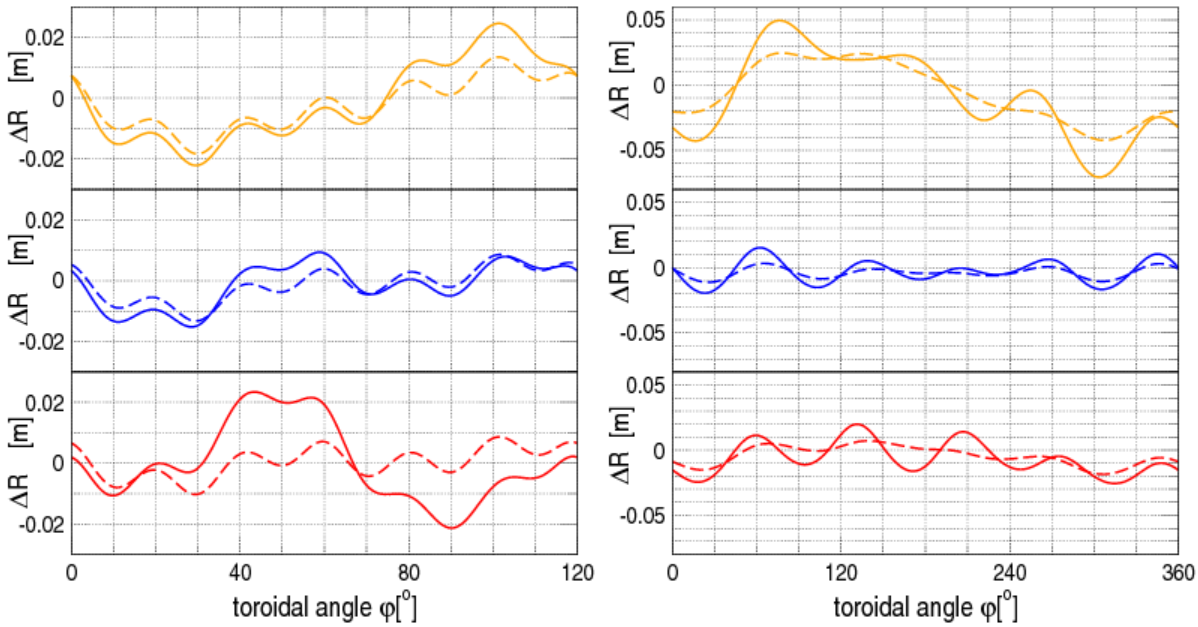


**Figure 48.** The midplane plasma boundary displacement as predicted by NEMEC for the (top pane) ITER 9MA scenario, (centre pane) 15MA L-mode phase and (bottom pane) 15MA H-mode phase as modelled with ASTRA when 90kAt is assumed in the in-vessel control coils in (left) $n = 3$ configuration and (right) $n = 4$ configuration.

### *7.3. Resistive MHD modelling*

Finally, nonlinear resistive MHD simulations have also been performed for the 15MA ITER baseline scenario with two different codes: M3D-C[1] and JOREK. In principle, these models represent the most accurate representation of the empirical situation and should therefore give greatest fidelity to the experiment and have greatest weight in the prediction for ITER, although the uncertainties in various parameters and profiles which influence the results strongly means that the prediction for ITER comes with large error bars.

Figure 49 shows the radial displacement across the pedestal region when $n = 1, 2, 3, 4$ RMPs are applied with maximum amplitude (ie $I_{IVCC} = 90$kAt) as predicted by linear M3D-C[1] simulations assuming various values for the pedestal-top temperature [41]. In all cases the boundary displacement increases with the pedestal temperature as the applied field is amplified by increasingly unstable low-$n$ peeling modes at the plasma edge. For the $n = 3$ and $n = 4$ configurations (as intended for ELM control) the boundary displacement can exceed 5cm for high pedestal pressures. However, it is important to note that the overlap criterion for the validity of linear simulations, $|\mathrm{d}\xi_r/\mathrm{d}r| < 1$, is violated for $T_{e,ped} = 5.1, 6.0$keV [41]. Nonetheless, even at $T_{e,ped} = 4.4$keV, which is assumed as the operating point for $Q = 10$ baseline scenario [64], both the $n = 3$ and $n = 4$ RMPs lead to a boundary displacement of $\pm\xi_a = 3.5$cm, or $\pm 1.75\%$ of the minor radius.

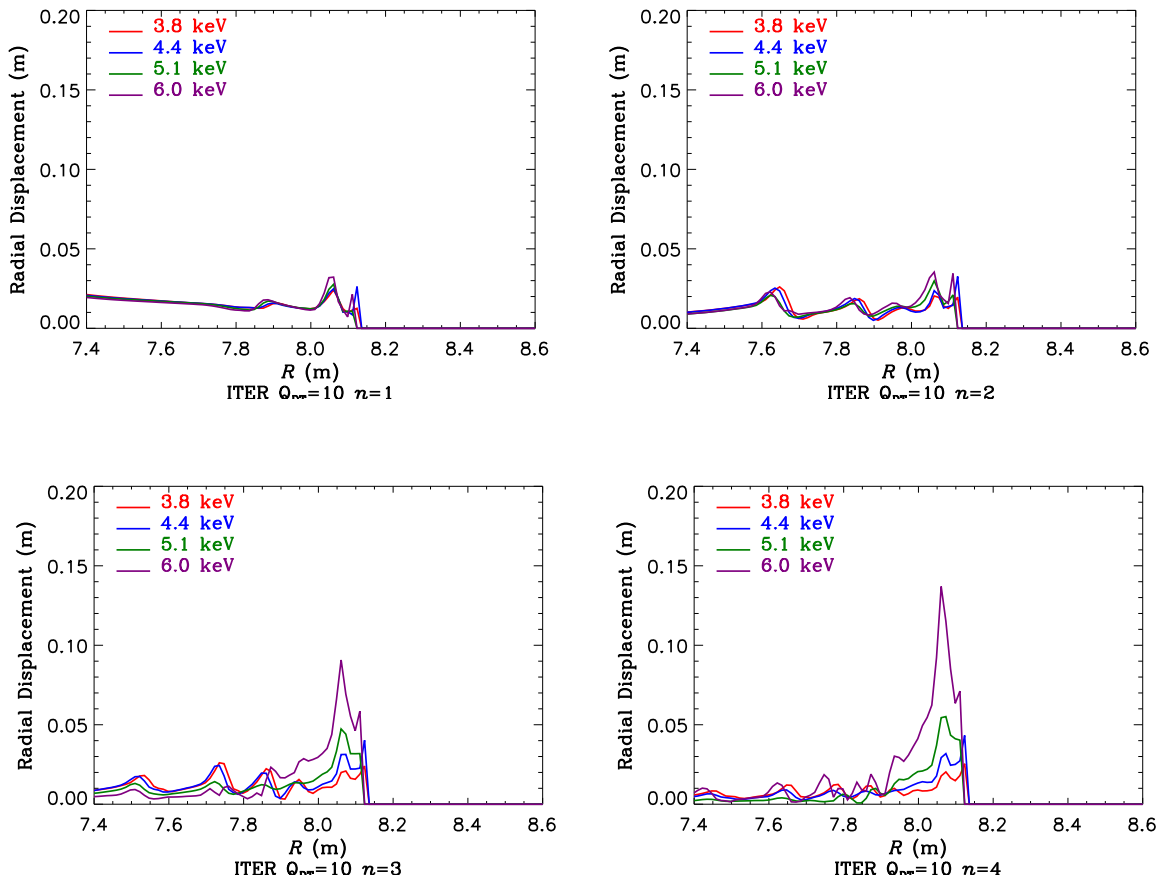


**Figure 49.** The radial displacement as a function of the major radius in ITER baseline H-mode scenario as predicted by the M3D-C[1] code when 90kAt is applied from the in-vessel coils in $n = 1, 2, 3, 4$ configurations, showing increasing displacement with pedestal temperature.

**** ADD TEXT HERE DEPENDING ON LATEST RUNS FROM NATE ****

The JOREK non-linear MHD code has also been used to simulate the effects of RMPs in ITER [42]. Figure 51 shows a Poincare plot of the magnetic field lines in ITER baseline scenario when diamagnetic flows and realistic toroidal rotation (left) are not included and (right) are included. The displacments near the X-point are significantly radially extended, but as figure 52 shows, the boundary displacements away from the X-point are negligible. Figure 53 shows the electron density and temperature profiles across the pedestal as predicted by JOREK when an $n = 3$ RMP is applied with $I_{IVCC} = 55$kAt, illustrating a boundary corrugation of $\pm 1$cm, ie only $\pm 0.5\%$ of the minor radius [42] (though of course this would be expected to approximately double at full applied field).

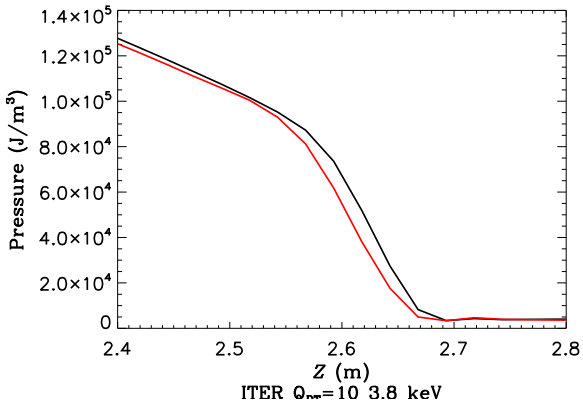


**Figure 50.** The electron pressure as a function of the vertical position at $R = 7.5$m as predicted by a non-linear M3D-C[1] simulation when 90kAt is applied in $n = 3$ configuration and a 3.8keV temperature pedestal is assumed.

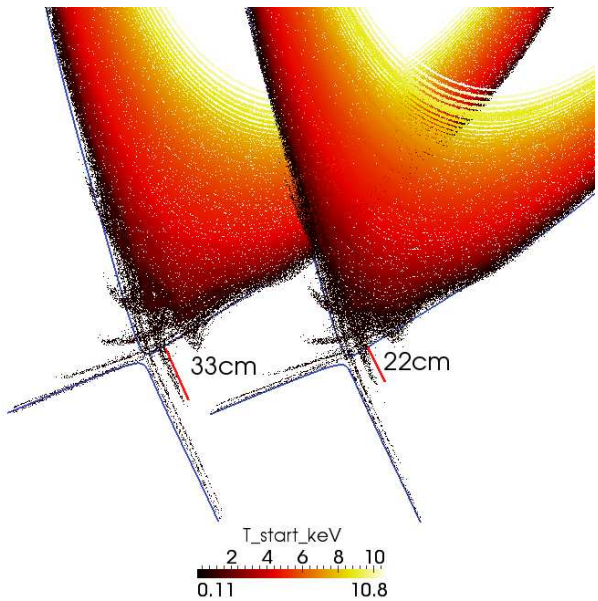


**Figure 51.** A Poincare plot of the magnetic field lines in ITER baseline scenario when diamagnetic flows and realistic toroidal rotation (left) are not included and (right) are included in JOREK, showing large displacements near the X-points.

## 8. Limitations and Future Work

### *8.1. Modelling*

Ideal 3d equilibrium reconstruction codes used in this study are limited to consider only nested magnetic surfaces and ignore possibly existing magnetic islands or stochastic regions. This could be recitified by using 3d equilibrium tools which do not assume

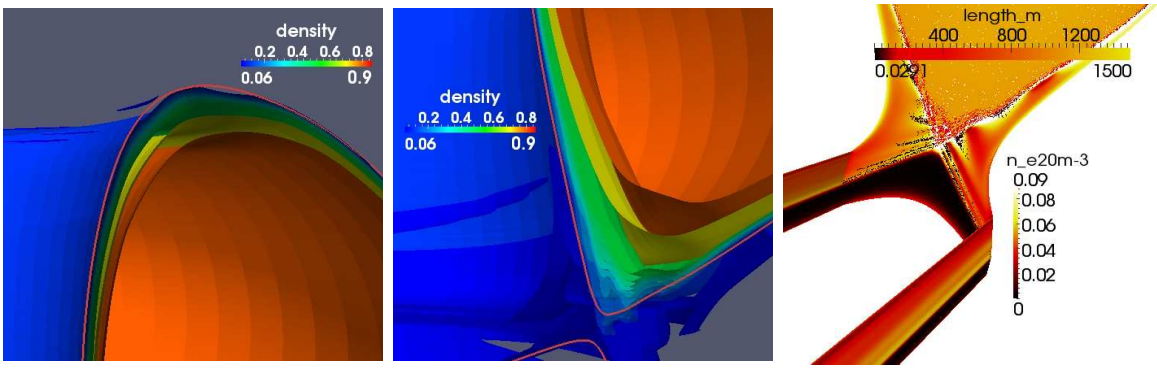


**Figure 52.** Poincare plots showing the (left) top, (middle) lower X-point region and (right) target of an ITER H-mode baseline plasma when 54kAt (half field) is applied in an $n = 3$ configuration as modelled with JOREK when realistic diamagnetic and toroidal flows are included.

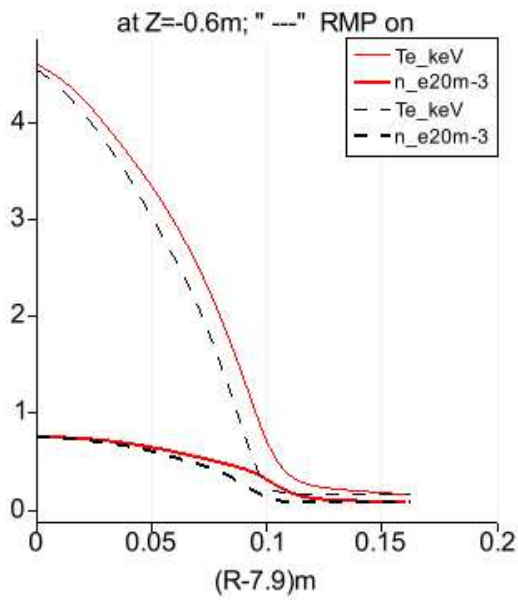


**Figure 53.** The electron density and temperature as a function of the minor radius as predicted by a non-linear JOREK simulation when 55kAt is applied in $n = 3$ configuration.

nested flux surfaces, such as HINT2 [59], PIES [60] or SPEC [61]. Furthermore, in its free-boundary version, VMEC uses the toroidal magnetic flux enclosed by the plasma boundary, $\Phi_{edge}$, as fixed quantity throughout the equilibrium iterations. This may lead to the assumption of magnetic surfaces where none are. This shortcoming of the VMEC approach can be dealt with by an iterative procedure in which $\Phi_{edge}$ in VMEC is varied according to the magnetic surface structure evaluated from the VMEC result by, for instance, the MFBE [62] or EXTENDER [63] codes.

### *8.2. Experiments*

The multi-machine database described in section 4.1 would require significantly more data to be reliable as an extrapolation tool; presently it shows a phenomenoligical trend from a limited dataset but extrapolation to ITER remains very uncertain. Furthermore, experiments which elucidate the interaction between the applied nonaxisymmetric fields and the plasma position controller, which in all modern day tokamaks relies upon data from one toroidal position, would be very valuable. Experiments which vary parameters which play a role in the plasma response could be very important; for instance assessing whether the value of $\beta_N/\beta_N^{no-wall}$ affects the corrugation, and subsequently developing scenarios accordingly to minimise the boundary deformation. Finally, the aim should be to demonstrate the application of RMPs (particularly rotating RMPs) with the position feedback taking data from multiple toroidal positions, as this report recommends for ITER. Further to this, reliable and consistent RF coupling should also be demonstrated in such plasmas with nonaxisymmetric position feedback schemes.

## 9. Discussion and Conclusions

It is evident that both saturated MHD instabilities and applied nonaxisymmetric fields can give rise to significant displacements of the plasma boundary. These displacements have been measured in various tokamaks and successfully compared with numerical simulation. Good agreement has been found between these experimental measurements and a range of models – from vacuum field line tracing, to ideal three dimensional MHD equilibrium reconstruction, to nonlinear plasma amplification – giving credence to the application of such simulations for extrapolation to ITER. The boundary displacement resultant from core MHD instabilities in ITER is predicted to be less than $\pm 1\%$ of the minor radius. Meanwhile, the RMP-induced displacements foreseen in ITER are expected to lie within the range of those predicted by the different models, meaning less than $\pm 1.75\%$ ($\pm 3.5$cm) of the minor radius in the H-mode baseline and less than $\pm 2.5\%$ ($\pm 5$cm) in a 9MA plasma.

Such toroidal corrugation of the plasma boundary affects many things, notably the coupling of ICRH, the minimum values of wall gaps assumed for safe operation, the plasma position control, and (de facto) the control of ELMs. Whilst a displacement of $\pm 3$cm in the baseline scenario is allowable from both a plasma control and heat loading perspective, it is important that ITER adopts a plasma control system which can account for a three dimensional boundary corrugation to avoid an $n = 0$ correction which would otherwise exacerbate the displacement caused by the applied fields.

**Acknowledgements**

This work was conducted under the auspices of the ITPA MHD Stability Topical Group. This work was partly funded by the RCUK Energy Programme [grant number EP/I501045]; the European Communities under the contract of Association between

EURATOM and CCFE, CEA, IPP, CRPP, FZJ and VR; and US Department of Energy under DE-XXXXXXXXX. The views and opinions expressed herein do not necessarily reflect those of the European Commission.

[1] Lao L *et al* 2005 *Proc. 47th Annual Meeting of Division of Plasma Physics (AIP)* CP1.00034
[2] R. Fischer *et al.* "Effect of non-axisymmetric magnetic perturbations on profiles at ASDEX Upgrade", 2011 *38th EPS Conference on Plasma Physics (Strasbourg)* P1.072 (http://ocs.ciemat.es/EPS2011PAP/pdf/P1.072.pdf)
[3] R Fischer et al, 2012, *Plasma Phys. Control. Fusion* **54** 115008
[4] J. C. Fuchs *et al.* "Influence of non-axisymmetric magnetic perturbations on the equilibrium reconstruction at ASDEX Upgrade", 2011 *38th EPS Conference on Plasma Physics (Strasbourg)* P1.090 (http://ocs.ciemat.es/EPS2011PAP/pdf/P1.090.pdf)
[5] Chapman IT *et al* 2007 *Nucl Fusion* **47** L36
[6] IT Chapman et al, 2012 *Plasma Phys Control Fusion* **54** 105013
[7] Lanctot MJ *et al* 2011 *Phys Plasmas* **18** 056121
[8] Kocan M, 2013 "Heat loads to the ITER first-wall panels in the ICRH-optimized plasma equilibrium" Tech. rep. ITER DML5YK
[9] JB Lister, A Portone and Y Gribov 2006 *Control Systems* **26** 79
[10] Chapman IT *et al* 2010 *Nuclear Fusion* **50** 045007
[11] Buratti P *et al* 2010 *Nuclear Fusion* **52** 023006
[12] Kwon OJ *et al* 2012 *Plasma Physics and Controlled Fusion* **54** 045010
[13] Menard JE et al, 2006 *Phys. Rev. Lett.* **97** 095002
[14] W. Chen, et. al., *Nucl.Fusion* **50** (2010) 084008
[15] Baruzzo M et al, 2010 *Plasma Phys. Control. Fusion* **52** 075001
[16] La Haye RJ et al. 2002 *Phys plasmas* **9** 2051
[17] Maraschek, M., et al 2003 *Plasma physics and controlled fusion* **45** 1369
[18] Garofalo, AM et al. 2007 *Nuclear Fusion* **49** 1121
[19] Sabbagh, SA, et al. 2010 *Nuclear Fusion* **50** 025020
[20] Katsuro-Hopkins, O et al. 2007 *Nuclear Fusion* **47** 1157
[21] J.W. Berkery, et al., *Phys Rev Lett* **104** (2010) 035003
[22] Bolzonella, T et al. 2008 *Physical Review Letters* **101** 165003
[23] Menard JE et al, 2005 *Nucl. Fusion* **45** 539
[24] Sabbagh SA et al, 2010 *Nucl. Fusion* **50** 025020
[25] Graves JP et al. 2013 *Plasma Phys. Control. Fusion* **55** 014005
[26] Cooper WA et al, 2011 *Plasma Phys. Control. Fusion* **53** 074008
[27] WA Cooper et al, *Plasma. Phys. Control. Fusion* **53** (2011) 024002
[28] WA Cooper et al, *Plasma Phys. Control. Fusion* **53** (2011) 124005
[29] Cooper WA *et al* 2009 *Comput. Phys. Commun.* **180** 1524
[30] Hirshman SP and Lee DK 1986 *Comput. Phys. Commun.* **43** 143
[31] Cooper WA et al, 2013 *40th EPS Conference on Plasma Physics, Helsinki, Finland*
[32] S. C. Jardin, J. Breslau, N. Ferraro, *J. Comput. Phys* **226** (2007) 2146
[33] Breslau JA et al, 2011 *Nucl. Fusion* **51** 063027
[34] O. Sauter, C. Angioni and Y.R. Lin-Liu *Phys. Plasmas* **6** 2834 (1999)
[35] O. Sauter, C. Angioni and Y.R. Lin-Liu *Phys. Plasmas* **9** 5140 (2002)
[36] D Yadykin et al, *sub Plasma Phys Control Fusion* 2013 "Effect of the external helical fields on the plasma boundary shape in JET"
[37] L. Frassinetti et al, *Rev. Sci. Instrum.* **83** (2012) 013506
[38] Nardon E. 2007 Edge Localized modes control by resonant magnetic perturbations PhD Thesis Ecole Polytechnique http://www.imprimerie.polytechnique.fr/Theses/Files/Nardon.pdf
[39] JM Canik et al, *Nucl. Fusion* **52** 054004 (2012)

[40] TM Bird and CH Hegna, *Nuclear Fusion* **53** 013004
[41] NM Ferraro et al, *24th IAEA Fusion Energy Conference, San Diego, USA* TH/P4-21 (2012)
[42] M Becoulet et al, *24th IAEA Fusion Energy Conference, San Diego, USA* TH/2-1
[43] Moyer, RA, et al. *Nuclear Fusion* **52** (2012) 123019
[44] Ferraro NM, *Phys. Plasmas* **19** 056105 (2012)
[45] Spong DA et al, *Nucl Fusion* **41** 711 (2011)
[46] Lazerson SA et al, *39th EPS Conference on Plasma Physics, Stockholm, Sweden* 2012
[47] Kirk A et al, 2013 *Nucl. Fusion* **53** 043007
[48] D Orlov et al. *Proc. 53rd Annual Meeting of Division of Plasma Physics (AIP)* Poster GP8.77 (2012)
[49] GTA Huysmans et al, *Plasma Phys Control Fusion* **51** 124012 (2009)
[50] Evans T *et al* 2005 *J Phys: Conf Ser* **7** 174
[51] Wingen A *et al* 2009 *Nucl Fusion* **49** 055027
[52] Kirk A *et al* 2012 *Phys Rev Letters* **108** 255003
[53] Jakubowski MW *et al* 2009 *Nucl. Fusion* **49** 095013
[54] Nardon E *et al* 2011 *J. Nucl. Materials* **415** S914
[55] Cahyna P *et al* 2011 *J. Nucl. Materials* **415** S927
[56] Schmitz O *et al* 2008 *Plasma Phys Control Fusion* **50** 124029
[57] Casper T et al, 2012 *24th IAEA Fusion Energy Conference, San Diego, USA* ITR/P1-15
[58] Gribov Y and Loarte A 2012 "Curents in ELM coils for edge plasma shape perturbation studies" Tech. rep. ITER 98BA5X
[59] T Hayashi, T Sato and A Takei, 1990 *Phys Fluids B* **2** 392
[60] A Reiman and H Greenside, 1990 *J Comput Physics* **87** 349
[61] S.R. Hudson, R.L. Dewar, M.J. Hole and M. McGann, 2012 *Plas. Phys. and Cont. Fusion* **54** 014005
[62] Strumberger E 1997 *Nucl. Fusion* **37** 19
[63] Drevlak M, Monticello D and Reiman A 2005 *Nucl. Fusion* **45** 731
[64] S Saarelma et al, *Nuclear Fusion* **52** 103020 (2012)